A framework for experimental determination of localised vertical pedestrian forces on full-scale structures using wireless attitude and heading reference systems

M. Bocian[1], J.M.W. Brownjohn[2], V. Racic[3,4], D. Hester[5], A. Quattrone[6], R. Monnickendam[2]

[1]Department of Engineering, University of Leicester, University Road, LE1 7RH, Leicester, UK

[2]Vibration Engineering Section, College of Engineering, Mathematics and Physical Sciences, University of Exeter, North Park Road, EX4 4QF, Exeter, UK

[3]Department of Civil and Structural Engineering, University of Sheffield, Mappin Street, S1 3JD, Sheffield, UK

[4]Department of Civil and Environmental Engineering, Politecnico di Milano, Piazza Leonardo da Vinci, 32, 20133 Milano, Italy

[5]School of Planning, Architecture and Civil Engineering, Queen's University Belfast, Stranmillis Road, BT9 5AG, Belfast, Northern Ireland

[6]Department of Structural and Geotechnical Engineering, Politecnico di Torino, 24 Corso Duca degli Abruzzi, 10129 Torino, Italy

Contact author: Dr Mateusz Bocian
                 Department of Engineering
                 University of Leicester
                 University Road
                 Leicester, LE1 7RH, UK
                 E-mail: m.bocian@leicester.ac.uk
                 Phone: +44 (0) 116 252 2539

Abstract

A major weakness among loading models for pedestrians walking on flexible structures proposed in recent years is the various uncorroborated assumptions made in their development. This applies to spatio-temporal characteristics of pedestrian loading and the nature of multi-object interactions. To alleviate this problem, a framework for the determination of localised pedestrian forces on full-scale structures is presented using a wireless attitude and heading reference systems (AHRS). An AHRS comprises a triad of tri-axial accelerometers, gyroscopes and magnetometers managed by a dedicated data processing unit, allowing motion in three-dimensional space to be reconstructed. A pedestrian loading model based on a single point inertial measurement from an AHRS is derived and shown to perform well against benchmark data collected on an instrumented treadmill. Unlike other models, the current model does not take any predefined form nor does it require any extrapolations as to the timing and amplitude of pedestrian loading. In order to assess correctly the influence of the moving pedestrian on behaviour of a structure, an algorithm for tracking the point of application of pedestrian force is developed based on data from a single AHRS attached to a foot. A set of controlled walking tests with a single pedestrian is conducted on a real footbridge for validation purposes. A remarkably good match between the measured and simulated bridge response is found, indeed confirming applicability of the proposed framework.

1 Introduction

Modelling the behaviour of lightweight structures due to the presence of active human occupants is a major challenge in the structural engineering community. The complexity arises owing to the highly adaptive nature of human behaviour and the potential of lightweight structures for dynamic response due to footfall loads, known as ground reaction forces (GRFs). Both of these conditions can lead to human-structure interaction phenomena and emergent crowd behaviour, which might influence dynamic structural stability. Human-structure interaction refers to a feedback loop in which the energy is transferred between two dynamical systems – a human and a structure. Emergent crowd behaviour refers to the ability of a crowd to exhibit complex behaviours, resulting from simple local interactions between crowd members. Because of this complexity, the behaviour of an individual pedestrian must be first understood in order to build a reliable crowd-structure system model, including any relationships between the components of the system.

1.1 Background

Significant progress on this topic has been made in recent years by looking for inspiration in other fields of science, traditionally seen as unrelated to structural engineering. Physics-based, biomechanically-inspired modelling of pedestrian loading has revealed plausible mechanisms of pedestrian-structure interaction [1–5], some already supported by direct empirical evidence from laboratory investigations [6–8] and indirect evidence from measurements and modelling studies on full-scale structures [2]. Further progress is being made by turning attention to and drawing from achievements in the field of cognitive science. It is becoming evident that, in order to capture natural pedestrian behaviour, the experimental conditions during laboratory trials must closely resemble real life experience [8,9]. However, while this approach can help to understand adaptations in pedestrian gait invoked by the presence of structural motion, it does not provide any information about the behaviour of a pedestrian in a crowd. Resolution of this issue has been long overdue in the field of research concerned with the dynamic stability of structures.

Although increasingly sophisticated mathematical models of pedestrian-structure interaction and crowd dynamics appear regularly in scientific literature [10–12], most of them suffer from lack of hard evidence to support their main assumptions. This is particularly true for numerous models of synchronisation of walking pedestrians to structural motion or to each other, which are the most often purported mechanisms responsible for the build-up of large amplitude structural vibrations. This problem has persisted due to lack of suitable technology allowing pedestrians' and structural behaviour to be measured simultaneously in situ [13]. As a result, loading models are usually derived and extrapolated to real life structures based on laboratory test data, most often collected while walking on a rigid surface in an environment offering

81 incongruent sensory information and preventing a test subject to freely adjust their gait. These limitations

82 can be argued to be the root cause of instability of the London Millennium Footbridge [14].

83 To address the abovementioned limitations of current modelling approaches a few attempts have been

84 made in recent years to develop a suitable framework for capturing pedestrian behaviour in situ. Two

85 main technology trajectories are being explored – optical motion capture systems (MCS) and wireless

86 inertial measurement units or monitors. These monitors, when using a fusion algorithm to compute global

87 orientation (i.e. relative to the direction of gravity and Earth's magnetic field) from a triad of

88 accelerometers, gyroscopes and magnetometers along with motion data, are referred to as Attitude and

89 Heading Reference Systems (AHRS), and a single monitor is *an* AHRS. An optical MCS, managed by a

90 dedicated data processing unit, consists of cameras tracking coordinates of markers.

1.2 Recent advances in in-situ measurement of pedestrian forces

91

92 The applicability of wireless AHRS for characterising pedestrian walking forces was studied by Van

93 Nimmen *et al.* [15]. In their modelling framework acceleration data from an inertial monitor attached at

94 pedestrian waist level were used to obtain information on timing of footsteps. Subsequently, the loading

95 model proposed by Li *et al.* [16] was fitted for the duration of each single step. This model relies on

96 summing five Fourier components representative of mean pacing frequency and its higher harmonics,

97 with amplitudes scaled in proportion to the walker body mass. Although the approach (i.e. attempting in-

98 situ measurement of pedestrian forces on a real structure) is an advance on earlier work in the area, some

99 limitations remain. For example, assigning a simple load shape function based on Fourier decomposition,

100 even if implemented when footstep onset is not periodic, introduces certain artificial repeatability and

101 neglects genuine time and amplitude variability present in force patterns, some of which can be associated

102 with human-structure interaction. Some concerns were acknowledged by the authors of [15] during a

103 discussion of findings from a series of controlled loading tests where up to six pedestrians walked on a

104 full-scale footbridge. It was noted that, for the single record of vertical response presented, when the

105 reconstructed force from four pedestrians (calculated using the proposed load modelling framework) was

106 applied to a numerical model of the bridge, the vertical response levels were three times those measured.

107 While there was some uncertainty about the modal characteristics of the footbridge used for the test, the

108 main source of discrepancy was assigned to human behaviour and shortcomings of the adopted loading

109 model [16]. Another possible source of simulation error is that walker position was inferred using an

110 assumed constant walking velocity, calculated from bridge length and test duration. Accurately knowing

111 the position of the walker is important as the modal force estimation requires the instantaneous amplitude

112 of pedestrian loading to be modulated by the localised mode shape amplitude.

113 More recently recommendations have been made by Dang & Živanović [17] as to a marker model for

114 reconstructing pedestrian vertical force using an inverse dynamics procedure [18] based on data collected

from an optical MCS in laboratory conditions. In short, this procedure relies on division of the human body into a number of interconnected segments of known length and position. The mass and position of the centre of mass is then determined for each segment based on anthropometric data, allowing the motion of the centre of mass (CoM) of the whole body to be calculated, from which the force is obtained in line with Newton's second law of motion. Dang & Živanović [17] found that, for stamping on a spot on a force plate, a model consisting of 19 markers was able to yield an absolute error in the amplitude of the component of force at the fundamental stamping frequency, against the directly measured force, of up to 15% in 90% of the trials. Additional tests were conducted during which a subject walked on a treadmill placed at the midspan of a flexible bridge. The absolute error in the average peak-per-cycle bridge response acceleration reconstructed based on the model, against the measured response, was up to 20% in 92% of the trials.

There are several practical drawbacks in using an optical MCS for measuring pedestrian kinematic data outdoors for pedestrian force reconstruction. Covering the volume of interest, e.g. the whole length of a footbridge, requires many cameras, at considerable economic and time cost [19,20]. Marker occlusion from fellow occupants of the structure and features of the environment is also a problem since, for optimal performance, all markers need to remain visible to at least two cameras at all times. Lighting conditions are a major problem, especially cloud cover alternating with strong sunlight, and operation of systems using active infrared light can be seriously compromised by fictitious data resulting from infrared components of solar radiation. Because of these limitations and due to growth in technology for personal instrumentation, for field work, a system using AHRS is advantageous.

1.3 The scope of this study

The goal of this study is to develop a framework for determining the localised vertical component of GRF on a structure in-situ while avoiding any rebuttable presumptions of the pedestrian behaviour. This could provide the means to calibrate both deterministic and stochastic models of GRFs of individuals and crowds along with structural response, and to investigate the interaction phenomena pertaining to the crowd-structure system, which could be critical for dynamic structural stability. Wireless AHRS were chosen due to practical advantages in system deployment, compact size and ease of use in the field.

The rest of the paper is organised as follows. Section 2 presents a study conducted to corroborate a pedestrian vertical force model based on a single point inertial measurement acquired with an AHRS. A pedestrian dead reckoning algorithm used to reconstruct the instantaneous position of pedestrian's foot based on data from a foot-mounted AHRS is then described in section 3. Another algorithm is proposed in section 3, which allows origin of the GRF vector (oGRF) to be located. Section 4 is concerned with a controlled pedestrian loading test performed on a 109 m long cable stayed footbridge to gather data allowing the proposed modelling framework to be validated. A study aiming at verifying the response

149 obtained using the proposed framework against the measured responses is presented in section 5.
150 Concluding remarks are presented in section 6.

151 **2   Pedestrian loading model based on a single point inertial measurement**

152 The first step in formulating the proposed framework was to evaluate whether a single point inertial
153 measurement could be used to reproduce pedestrian vertical force in enough detail for it to be suitable for
154 use in structural loading models. With this aim in mind, a dedicated experimental campaign was
155 conducted during which test subjects instrumented with AHRS and also monitored with an optical MCS
156 performed walking tests on an instrumented treadmill located in the Light Structures Laboratory of the
157 University of Sheffield, UK. The data obtained from the treadmill were used to benchmark the loading
158 model. The study was approved by the University of Sheffield Research Ethics Committee.

159 **2.1   Overview of the experiments**

160 Six subjects (S1-S6), all healthy British male adults in their early twenties, participated in the study. Their
161 basic anthropometric data are given in Table 1. All subjects had prior experience with walking on a
162 motorised treadmill, all signed an informed consent form and all completed a physical activity readiness
163 questionnaire.

164 Table 1 Basic data for all experimental subjects for tests conducted on an instrumented treadmill.

Subject ID	S1	S2	S3	S4	S5	S6
Mass m_p [kg]	90	75	81	60	93	64
Height h [m]	1.83	1.80	1.90	1.79	1.88	1.74
Age [years]	21	22	21	22	21	21

165

166 Each subject wore gym-type shoes and tight-fitting gym clothes allowing AHRS to be placed at four
167 specific locations on their body, namely seventh cervical vertebra (neck), sternum, navel and fifth lumbar
168 vertebra (lower back), as can be seen in Figure 1. At least 8 minutes of habituation to the experience of
169 walking on the treadmill in the laboratory environment was given to each subject. Each subject then
170 participated in six walking tests in which the imposed speed of treadmill belts was typically between 0.6
171 and 1.4 ms^{-1}. The choice of the speed was determined by first allowing the subject to establish a
172 comfortable speed, and then varying the speed in approximately 10% increments, such that there was one
173 speed faster than comfortable and four speeds slower. While speeds faster than 1.4 ms^{-1} have been
174 observed among pedestrians walking on real structures [21], this upper speed limit was imposed for
175 experimental protocol to comply with the requirements of the University of Sheffield Research Ethics
176 Committee, to prevent tests subjects from discomfort. Each test lasted for approximately three minutes,
177 which, after discarding periods associated with gait and instrumentation initiation and termination stages,

178 allowed approximately two minutes of data to be obtained for further processing. To prevent bias due to

179 subject's predictive behaviour and account for the change of behaviour with time e.g. due to fatigue, the

180 order of tests was randomised.

(a)   (b)   (c)
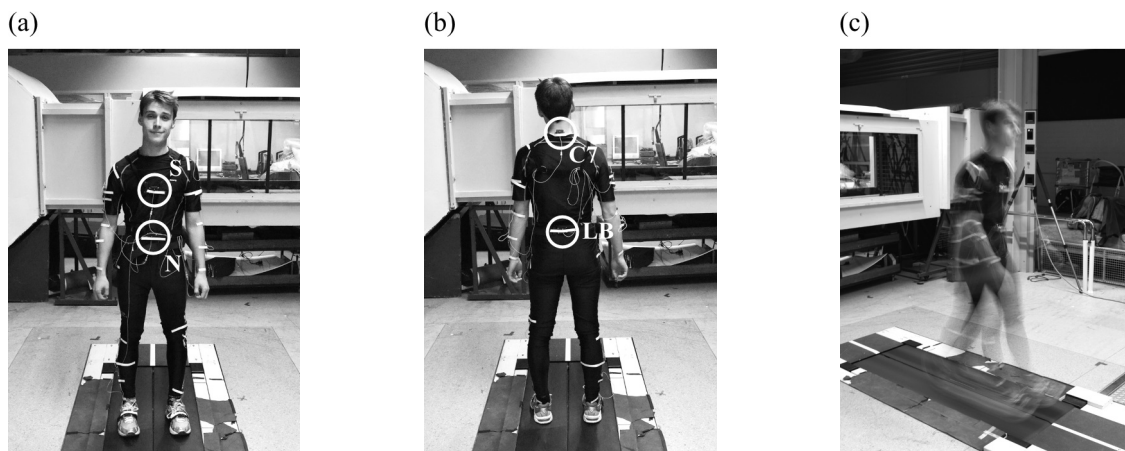
181 Figure 1 (a) Opal^{TM} AHRS monitors attached at the sternum (S) and navel (N) levels (b) Opal^{TM} AHRS

182   attached at the fifth lumbar vertebra (lower back; LB) and seventh cervical vertebra (neck;

183   C7). (c) A subject during a walking test on a split-belt instrumented treadmill.

2.2   Instrumentation

185 Three independent instrumentation systems were deployed during the experiments – an ADAL3D-F split-

186 belt instrumented treadmill [22], wireless APDM Opal^{TM} monitors [23] and Codamotion optical MCS

187 [24]. The analyses presented in this section are based on data from the former two systems only and their

188 relevant specifications are given in more detail. The MCS mainly functioned as a data acquisition system,

189 simultaneously recording force data from the treadmill and triggers generated by the wireless system in

190 the form of sharp voltage spikes, allowing the beginning and end points of their signals to be identified

191 within treadmill data.

2.2.1   Instrumented treadmill

193 The vertical forces exerted by a pedestrian on the walking surface were measured directly by the

194 ADAL3D-F which incorporates a force plate under each of the two parallel treadmill belts. Built

195 specifically for clinical gait analysis, the treadmill is stiff enough not to cause pollution of the measured

196 signals with errors due to resonance and flexure. The data from the treadmill calibrated to engineering

197 units of force were acquired via proprietary software at a rate of 1 kHz.

2.2.2   Wireless AHRS

199 Six APDM Opal^{TM} AHRS and a wireless access point allowed real-time wireless data streaming and

200 communication with a host computer. Each AHRS (or *monitor*), based on Micro-Electro-Mechanical

201   System (MEMS) technology, incorporates triaxial magnetometer sensing orientation against the direction

202   of a magnetic field, triaxial accelerometer, and a triaxial gyroscope sensing rate of change of rotation, and

203   a temperature sensor. In order to recover motion in three-dimensional space, the sensors axes form a right

204   handed triad. AHRS resources are managed by a microcontroller and wireless communication is achieved

205   with a radio module. In the laboratory treadmill tests monitor data were streamed wirelessly to a host

206   computer, although each monitor also contains on-board flash memory allowing direct logging, a feature

207   used during tests on a full-scale structure reported in section 5. Opal^{TM} monitors are different from

208   *inertial measurement units* which provide data on translational and rotational movements only. This is

209   because Opals^{TM} incorporate a magnetometer, which allows their orientation to be determined relative to

210   the Earth's gravity and magnetic field [25].

211   Proprietary software of APDM (Motion Studio, version 1.0.0.2015) was used for system calibration and

212   data retrieval. All monitor data were sampled at 128 Hz and, since the force amplitude for the chosen

213   conditions was not expected to exceed twice body weight, accelerometer operational ranges were set to 2

214   g.

215   **2.3   Data processing**

216   The main goals of data processing were to derive a pedestrian vertical loading model based on AHRS

217   data and to benchmark this model against the vertical component of pedestrian GRF measured from the

218   treadmill. This section describes procedures adopted in order to realise these goals and establishes quality

219   indicators for evaluation of the proposed pedestrian loading model.

220   **2.3.1   Treadmill data**

221   After correcting for the drift associated with piezoelectric effect exploited by the force transducers,

222   calibrated treadmill data were aligned with AHRS data using triggers recorded by the wireless system

223   (see section 2.2). All data were set to a common sampling rate of 128 Hz. A delay-compensated

224   antialiasing finite impulse response low-pass filter was used in down-sampling data from the treadmill.

225   Exemplar calibrated force traces from the right and left leg corrected for drift are shown in Figure 2. All

226   data are unfiltered and for S2 walking at 1.28 ms^{-1}. Take-off (TO) and touch-down (TD) events at which

227   the foot loses and regains contact with the ground, respectively, were detected in the drift-corrected data.

228   This was necessary because reliable estimates of pedestrian force amplitudes in spectral calculations

229   require that the analysed record should contain an integer number of pedestrian walking cycles. A force

230   threshold of 10 N was chosen for these analyses. An exemplar application of this threshold for detection

231   of TD (circles) and TO (dots) is shown in Figure 2, for S2 walking at 1.28 ms^{-1}.
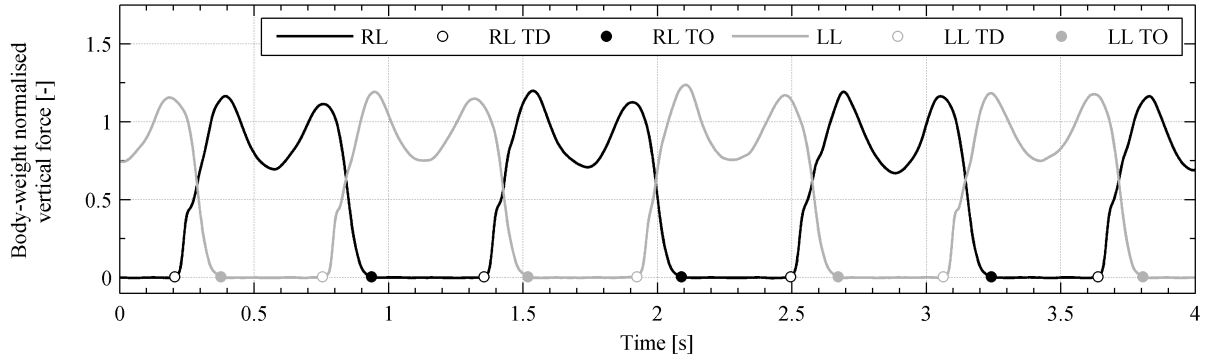
Figure 2 Exemplar body weight-normalised vertical pedestrian force from treadmill for right and left leg (RL and LL, respectively). Also denoted on the plot are touch-down (TD) and take-off (TO) events for both legs.

2.3.2 AHRS data used in the pedestrian vertical loading model

An underlying assumption in deriving a loading model based on a single point inertial measurement is that the recorded motion of the monitor represents the motion of the CoM of the whole body. A similar approach, albeit based on MCS data, was previously used in an attempt to reconstruct the lateral component of pedestrian force on laterally-oscillating ground [26], and human jumping forces [27]. The pedestrian force can be obtained directly by applying Newton's second law of motion:

$$F(t) = \underbrace{m_p g}_{\text{static force}} + \underbrace{m_p a_M(t)}_{\text{dynamic force}} \tag{1}$$

where m_p is the pedestrian mass, g is gravitational acceleration and a_M is the acceleration measured by a monitor. This assumption is substantiated for acceleration data from a monitor attached at waist level since, although not directly linked to any anatomical body landmarks, the CoM excursions in walking can be expected to fluctuate around the superior aperture of the pelvis [28]. However this cannot be assumed to be true for other monitor locations. Nevertheless, performance of this simple loading model was tested on data from monitors attached at four different locations on the subject's body: the fifth lumbar vertebra (lower back), navel, sternum and the seventh cervical vertebra (C7; neck), which are shown in Figure 1. Elastic straps were used to secure all monitors except when placed on C7 where the monitor was secured with medical-grade double-sided tape. The locations as well as the loading models that use monitors at these locations are referred to here as LB, N, S and C7, respectively.

For the loading model to be applicable it must provide the pedestrian force in a reference frame meaningful from the structural standpoint, yet each monitor senses acceleration in its local (i.e. monitor) coordinate system (LCS). Despite the most careful monitor placement, its orientation is bound to change while walking, hence alignment of one monitor axis with the vertical direction in world (i.e. Earth) coordinate system (WCS) cannot be guaranteed and must be resolved from LCS data. For each data set

9

257 associated with a single time stamp, each monitor encodes a four-dimensional complex number, known as

258 quaternion, representing monitor orientation against a magnetic North, West and vertical-up Earth

259 reference frame. The data in LCS were transformed to WCS using quaternion algebra [29].

2.3.3 Evaluating the pedestrian vertical loading model

261 For structural vibration serviceability, the most important component of pedestrian vertical force is at the

262 fundamental walking frequency, hence evaluation of the pedestrian loading model presented in this paper

263 mostly focuses on this force component. The evaluation of the data from the loading models is carried out

264 in sections 2.4 and 2.5 while the theory behind the evaluation process is briefly described below.

265 The proposed loading model assumes that monitor data represent motion of the CoM (see section 2.3.2)

266 hence the force reconstructed with Eq. (1) is the total pedestrian force. The corresponding total pedestrian

267 force from the treadmill was obtained by summing the force signals from both treadmill force plates (see

268 Figure 2), and the amplitude of the force component of interest was extracted from the Fourier magnitude

269 of force obtained using the procedure outlined in section 2.3.1.

270 In order to assess temporal congruence of the model with data obtained directly from the treadmill,

271 Fourier semblance was calculated [30]:

$$S_{T,M}(f) = \frac{\Re_T(f)\Re_M(f) + \Im_T(f)\Im_M(f)}{\left[\Re_T^2(f) + \Im_T^2(f)\right]^{0.5} \times \left[\Re_M^2(f) + \Im_M^2(f)\right]^{0.5}} \tag{2}$$

273 where f is the frequency, $S_{T,M}$ is the semblance between the force from the treadmill (denoted by

274 subscript T) and the force reconstructed based on Opal^{TM} acceleration data (denoted by subscript M),

275 and $\Re$ and $\Im$ denote the real and imaginary part of the complex Fourier coefficient. This approach is

276 more intuitive than simply stating phase difference in an angular scale since, similarly to the Pearson's

277 correlation coefficient, Eq. (2) returns values from –1 to +1, where –1 and +1 imply perfect out-of-phase

278 and in phase correlation, respectively, and 0 implies lack of correlation.

279 Performance of the loading model derived from Eq. (1) was assessed in statistical terms by estimating

280 empirical cumulative distribution functions. Absolute percentage error value in the amplitude of

281 pedestrian vertical force component at the fundamental walking frequency reconstructed based on

282 Opals^{TM} acceleration data, ΔF, was used as a quality indicator. It was calculated according to:

$$\Delta F = \left| \frac{F_T - F_M}{F_T} \right| \times 100\% \tag{3}$$

284 where F_T and F_M are the amplitudes of Fourier force components at the fundamental walking frequency

285 obtained from data from the treadmill and Opal^{TM} monitor, respectively.

2.4   Results and discussion

287 Results from analysis of data collected from the experimental campaign are reported in this section. The

288 data presented in section 2.4.1 relate to S2 ($m_p = 75\,\text{kg}$ and $h = 1.8\,\text{m}$) walking at 1.28 ms^{-1}. The choice

289 of this particular dataset was dictated by several factors. First, the walking velocity is close to the average

290 walking velocity measured on some footbridges (1.3 ms^{-1}) [21]. Second, the subject's mass and height are

291 close to the average values for the male English population aged 16-24 (74.8 kg and 1.776 m) [31].

292 Nevertheless, the relationships discovered in the data apply for all participants of the campaign.

2.4.1   Amplitude and timing

294 Exemplar truncated time histories of body-weight normalised vertical force measured directly by the

295 treadmill and reconstructed based on Eq. (1) are presented in Figure 3. Footbridge vibration serviceability

296 assessments rarely consider more than the first or second harmonics of pacing rate. However, to allow a

297 more detailed comparison between the forces measured by the treadmill and the forces predicted by the

298 loading model, a two-way second-order Butterworth low-pass filter with cut-off frequency 8 Hz was

299 applied to all the data. Part (a) of Figure 3 shows the force calculated from a monitor attached at the lower

300 back (LB) and navel (N), whereas part (b) shows the force calculated from a monitor attached at the

301 sternum (S) and neck (C7).

302

(a)

(b)
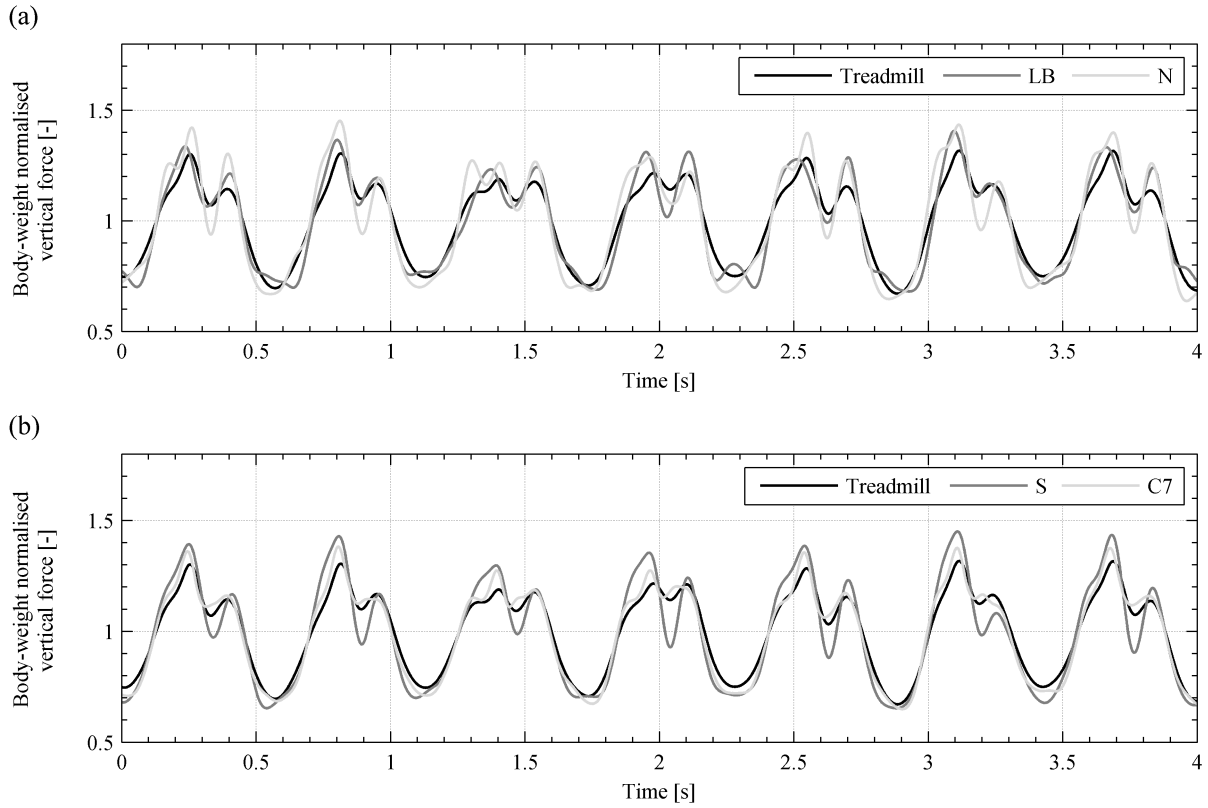
303 Figure 3 Truncated time histories of pedestrian total vertical walking force from direct measurement
304 (treadmill) and reconstructed based on acceleration acquired by monitors placed at (a) LB
305 and N and (b) S and C7.

306 Visual inspection reveals that the patterns of variation of the reconstructed forces (calculated from the
307 monitor data) resemble the characteristics of the force obtained from the treadmill, both in amplitude and
308 shape. A remarkably good match can be seen for model C7 and the worst match for model N. Variability
309 in the force amplitude is particularly pronounced for model S, indicating the presence of considerable
310 energy at higher frequency components.

311 Single-sided power-preserving FFT magnitudes of data in Figure 3, relieved of the static (0 Hz) force
312 component and taken over a longer interval, are presented in Figure 4. It can be seen in Figure 4 (a) & (b)
313 that the proposed loading model can capture (at least qualitatively) all components of pedestrian vertical
314 force, including those at $nf_p \pm 0.5f_p$, where f_p is the pacing frequency and n is a positive integer, which
315 are most likely associated with gait laterality [9]. Good agreement between the directly measured force
316 and the force reconstructed from the model around f_p is visible in Figure 4 (c) & (d). The spread of
317 energy into neighbouring force components is caused by adaptations in gait pattern throughout the test. In
318 most of the cases the accuracy of the loading model degrades for higher harmonics, most strongly for
319 model S. In contrast, Fourier amplitudes of force from model C7 give a remarkably good match with the
320 amplitudes of force measured directly on the treadmill, up to the fourth harmonic.
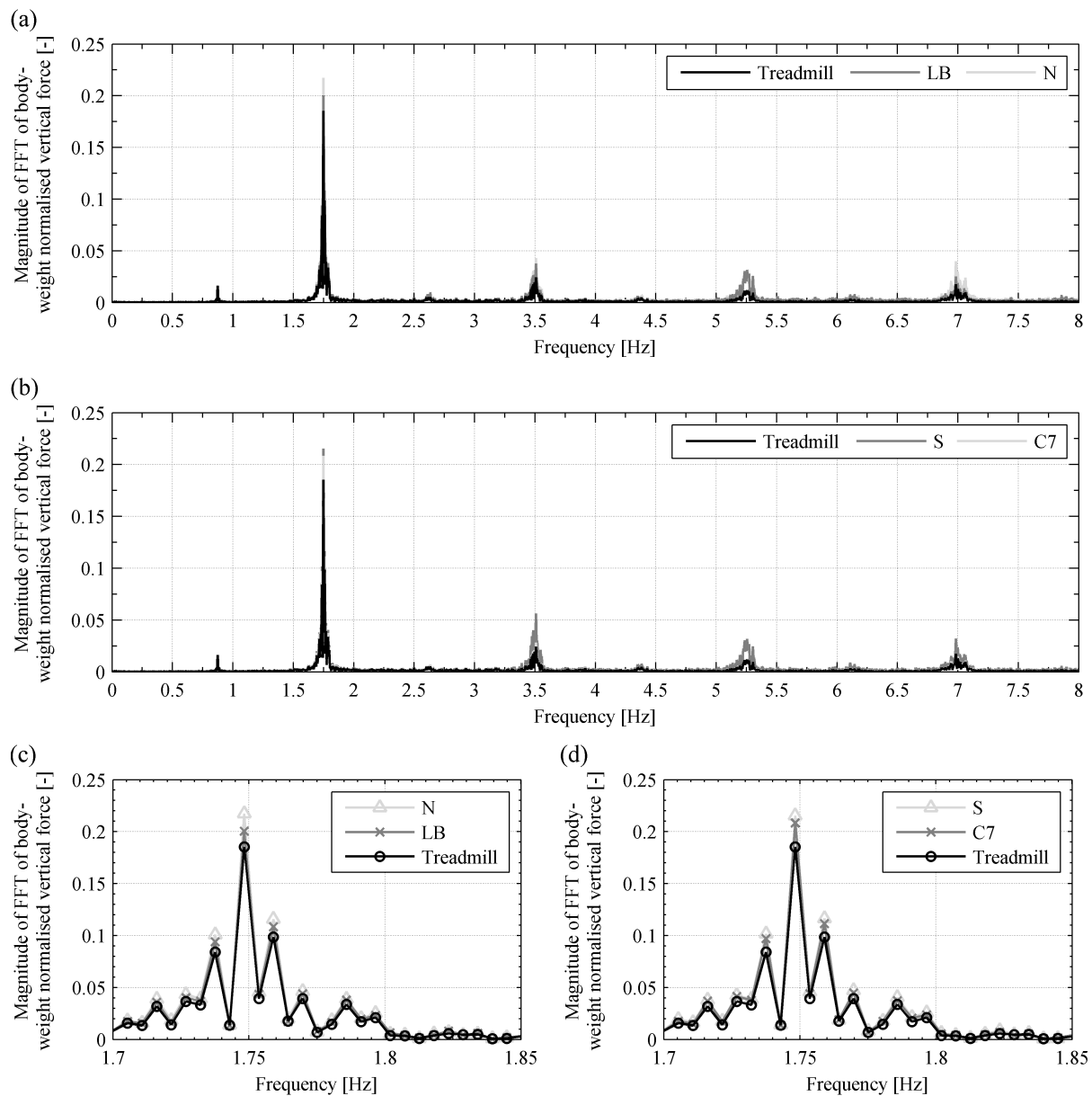
Figure 4 Single-sided power-preserving magnitude of FFT of body-weight normalised vertical force from direct measurement (treadmill) and reconstructed based on data from monitors placed at (a) LB and N and (b) S and C7. The amplitudes of force components around the fundamental walking frequency are shown in more detail in (c) and (d).

The overestimation of energy at higher frequencies is associated with noise in the kinematic data. This noise can arise due to soft tissue artefacts, slippage of the straps attaching monitors to subjects' bodies or interference of the monitor with underlying clothing. Better signal-to-noise ratio might explain why model C7, based on acceleration from a monitor attached directly to the skin with double-sided tape at the level of the seventh cervical vertebra, consistently outperformed other models.

The results of the analysis of data in Figure 4 for temporal similarity are presented in Figure 5. Reliable estimates of Fourier semblance are available for the components of force carrying significant spectral

332   energy. The most important of these components are at nf_p, where n is a positive integer. The

333   corresponding values of Fourier semblance are denoted by dots in Figure 5.

(a)

(b)

(c)

(d)
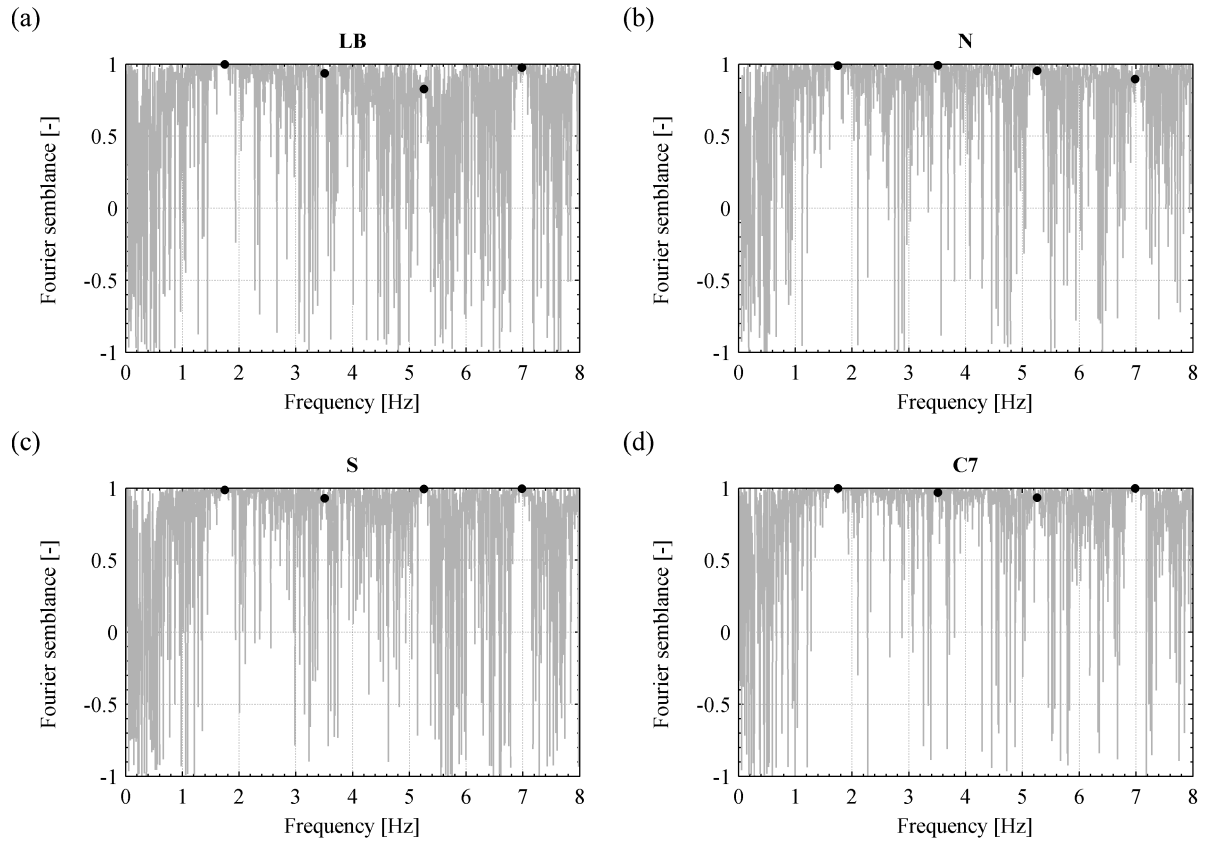
334   Figure 5 Fourier semblance between the force from direct measurement and reconstructed based on data

335   from monitors placed at (a) LB, (b) N, (c) S and (d) C7. Black dots denote the values

336   corresponding to the component of force at the fundamental walking frequency and its

337   harmonics.

338   In all cases time correlation in the component of force at the walking frequency obtained from the model

339   and the treadmill is almost perfect, but can diminish for higher harmonics. The best temporal congruence

340   can be seen for models S and C7. The aggregated measures of time correlation for the component of force

341   at the fundamental walking frequency, for all of the conducted tests from a model associated with each

342   monitor location, are given in Table 2.

343   Table 2 Mean Fourier semblance and phase difference for the component of force at the fundamental

344   walking frequency based on data reconstructed with the model and measured directly on the

345   treadmill. Values of standard deviation are given in brackets.

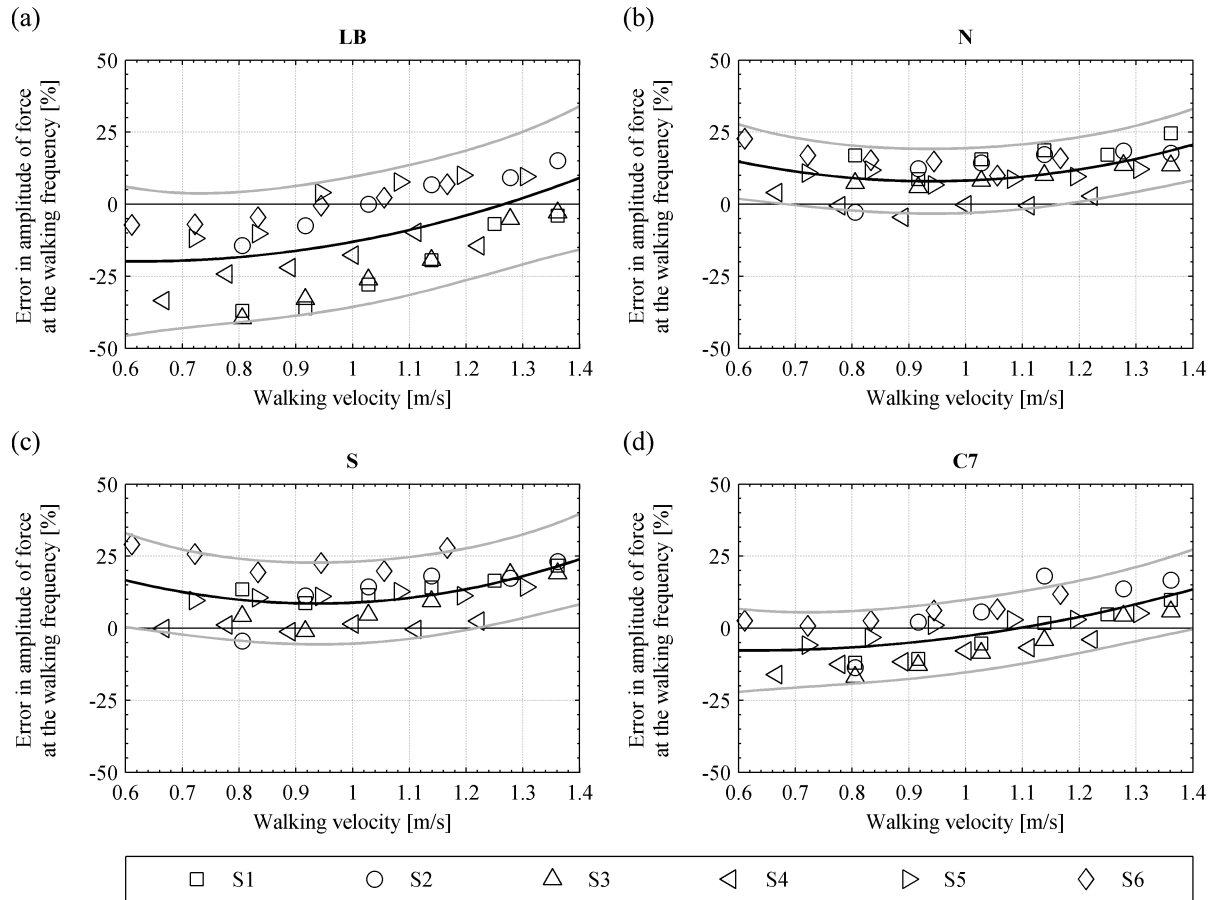| Model	LB	N	S	C7
Fourier semblance [n/a]	0.986 (0.024)	0.977 (0.028)	0.973 (0.032)	0.987 (0.022)
Phase difference [rad]	-0.022 (0.170)	0.161 (0.144)	0.182 (0.151)	0.076 (0.149)

346

347 The time correlation between the models and the treadmill data is generally strong, with mean Fourier
348 semblance above 0.97 and mean standard deviation up to 0.032. Directionality of this relationship is
349 indicated by the sign of mean phase difference. Model LB tends to lag data from the treadmill, but the
350 opposite is observed for all other models. Standard deviation of phase difference is generally similar.

2.4.2 The influence of walking velocity

352 The influence of walking velocity on the error in the predicted amplitude of the component of force at the
353 walking frequency is shown in Figure 6. Each plot contains data from all subjects (denoted by different
354 symbols) from all of the conducted tests, from a model associated with one monitor location. Since the
355 data in each plot show distinct ranges containing their minima and maxima, a best fit second order
356 polynomial is denoted on each plot as a black curve to show the data trend. To show significance of data
357 scatter, 90% pointwise confidence bounds for a new observation are denoted in grey.

358 Models N and S most often overestimate the measured force and their patterns of variation of the error are
359 similar, with the best fit curve in Figure 6 (b) for model N being almost linear within the range of the
360 presented data. Therefore this model can be used to obtain conservative estimates of pedestrian force in
361 vicinity of the fundamental walking frequency. Model N, for which the spread of data around the fit is
362 less than for model S, yields an average absolute error of 11%. Taking all the above into account it is
363 conceivable that model N, simply corrected for the offset by subtracting a constant, could be used to
364 obtain reasonable estimates of pedestrian force for different walking velocities. Model LB performs well
365 for normal walking speeds (i.e. above 1.2 ms^{-1}) yielding an average absolute error of 8% and maximum
366 error of 15%. However, it suffers from increasing inaccuracies with decreasing walking speeds, both in
367 terms of the mean error and its variability. A considerable dispersion of data for model LB might be
368 associated with flexing back extensor (*erector spinae*) and surrounding muscles during the gait cycle. The
369 strength of this effect is likely to be influenced by physiological composition of the tissue underlying the
370 monitor and attaching straps.

371 The best agreement with the directly measured force is found for model C7, yielding average absolute
372 error of 7.7% . However, Figure 6 (d) shows that the data from that model also lend themselves to a
373 curvilinear fit. The reliability of the pedestrian loading models derived from Eq. (1) is further discussed in
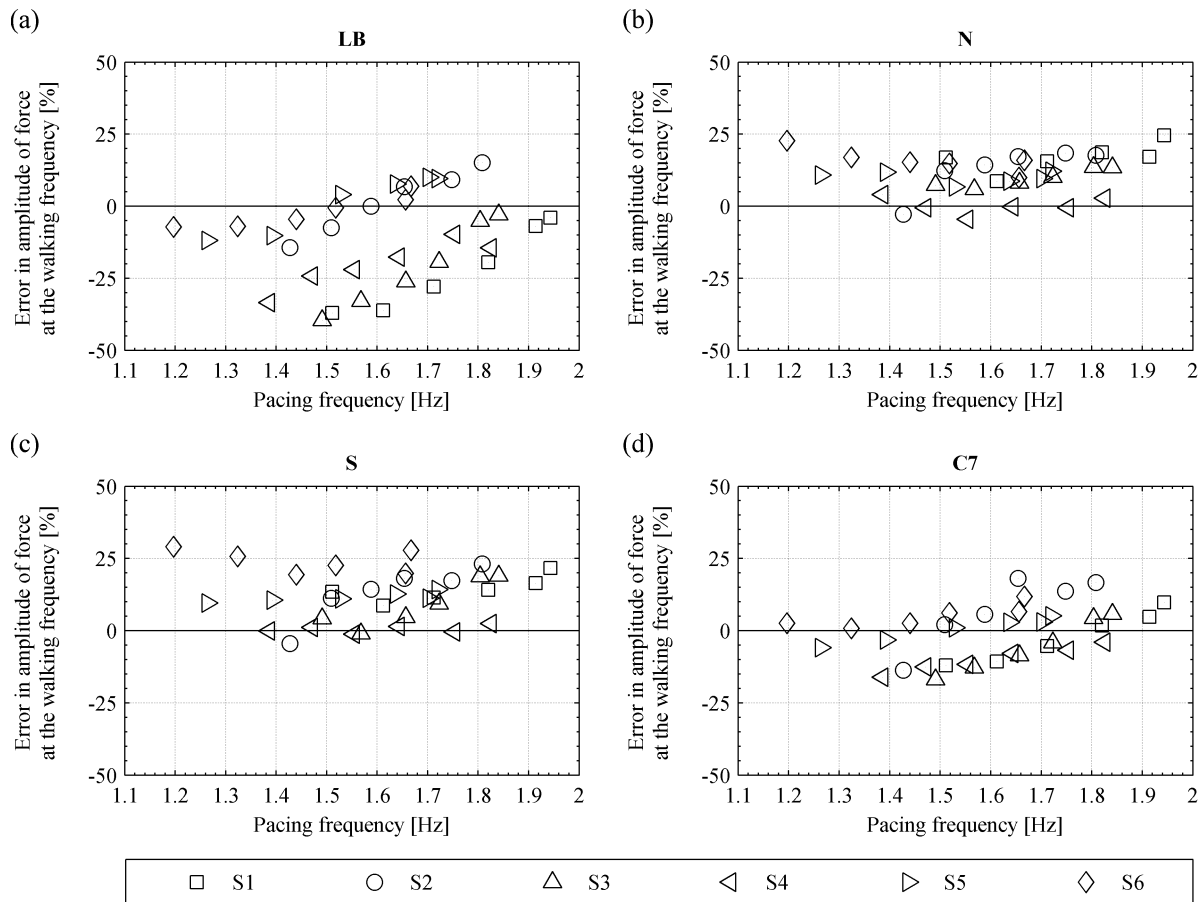374 section 2.5.

Figure 6 Percentage error in Fourier force amplitude at fundamental walking frequency against walking velocity, for all subjects and tests, for data from (a) LB, (b) N, (c) S and (d) C7. The best fit second order polynomial is also denoted on each plot as a black curve to show trends in the data, together with 90% pointwise confidence bounds denoted as grey curves.

Subject-dependent trends can be identified in the data, for example, all data for S1, S3 and S4 lie below the fit in Figure 6 (a), while all data for the other subjects lie above that fit. Interestingly, similar subject-dependant trends in the error of force amplitude can be observed in data reported in [17]. Since this effect appears to be systematic, it is most likely caused by different body mass distribution of test subjects and inaccuracies in monitor (or marker) placement. This can distort the estimated motion of the CoM representing overall body dynamics, used for reconstructing pedestrian vertical force in both studies.

2.4.3 The influence of pacing frequency

It is well known that pacing frequency and walking velocity have a strong correlation [32] so it is no surprise that plots of error in fundamental Fourier amplitude component of vertical force against the pacing frequency (Figure 7) show patterns resembling those errors plotted against walking speed (Figure 6). Furthermore, as in Figure 6, subject-dependent trends are visible in Figure 7.

16

Figure 7 The percentage error in Fourier force amplitude at the pacing frequency against that frequency, for all subjects and tests, for data from monitors placed at (a) LB, (b) N, (c) S and (d) C7.

2.5 Reliability of the pedestrian loading model

Rather than fitting a certain distribution to data and analytically evaluating confidence levels, reliability of the loading models was assessed by inspecting the empirical (non-parametric) cumulative distribution functions. Error in amplitude of the reconstructed force component at the fundamental walking frequency was used as a quality indicator (see section 2.3.3). The same methodology was adopted in [17]. The results of this assessment are presented in Figure 8.

Model C7 captures pedestrian loading relatively well, being able to achieve an absolute error below 15% at 90% probability of occurrence. Conversely, diminishing gradient of the cumulative distribution function for model LB indicates multiple outliers in the data, which correspond to lower walking speeds. Consequently, the overall performance of this model is relatively poor. Models N and S yield absolute errors below 18% and 23%, respectively, at 90% probability of occurrence. Note that a fixed treadmill was used in validating the models, but it is assumed with supporting evidence [33], that a compliant structure does not significantly affect this validation.

17
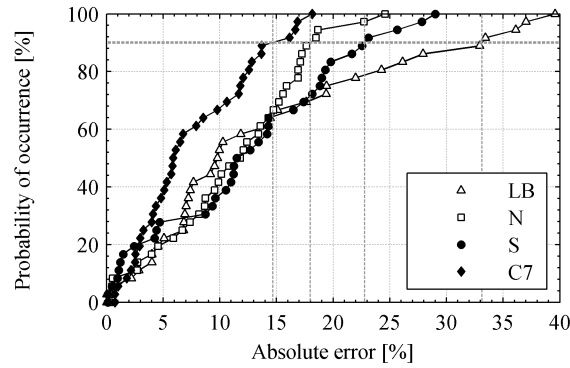
Figure 8 Empirical cumulative distribution functions for absolute percentage error value in the amplitude of pedestrian vertical force component at the pacing frequency, reconstructed based on data from LB, N, S and C7. The values of the error corresponding to 90% probability of occurrence are indicated via grey lines.

Considering the simplicity of the proposed model and the consistency in the relationships discovered in the experimental data, it can be concluded that pedestrian vertical force model based on a single point inertial measurement can capture the characteristics of walking forces with a quantified good accuracy. To obtain the most reliable estimates of pedestrian vertical force at different walking speeds, model C7 is recommended. Considering the results reported in [26] and [27], it can be concluded that model C7 is the best for monitoring human body kinetics for a range of activities. For walking at a comfortable speed (above 1.2 ms^{-1}) model LB can also be used, if only the components of force at and around the first harmonic are considered. Model N could be used directly to obtain conservative estimates of pedestrian force around the fundamental walking frequency. Alternatively, it could be modified by introducing a constant offset to better represent real forces. Note that the speeds imposed during the tests ranged from slow to comfortable, but the performance of the models for fast speeds (above 1.4 ms^{-1}) was not tested. The data trends in Figure 6 suggest that the errors could increase with speed, but this would require further tests for clarification.

3   Pedestrian force location tracking

Recommendations regarding the pedestrian force model based on a single point AHRS measurement were given in the previous section. However, in order to estimate correctly the influence of each pedestrian on bridge dynamics the location of the origin of the GRF vector (oGRF) needs to be established. Knowledge of pedestrians locations on a structure is also needed for analysing pedestrian-structure interaction, since the perceived vibration amplitudes depend on the local amplitude of the considered mode shape. The same information is required for analysing interactions between pedestrians, since the behavior of each pedestrian might be affected by the behavior of their neighbours. Therefore a detailed description of pedestrian force location tracking is given in this section. This work is timely as this issue has not been previously addressed in the context of research on human-induced vibration of

18

432 structures. Furthermore, previous attempts at tracking pedestrian location from video footage [34-37]
433 failed to accomplish this over long distances travelled by the pedestrians. Consequently assumptions of
434 instantaneous pedestrian location are commonly made in response simulations, with the oGRF taken as
435 equivalent to that position. The most common assumption is that of a linear relationship between mean
436 values of walking velocity, v, step frequency, f_p, and step length, d :

$$v = f_p d \qquad (4)$$

438 which neglects step-to-step variability. This can introduce inaccuracies in modal force estimation and
439 cause discrepancies between the modelled and measured dynamic response. To alleviate this problem an
440 algorithm for tracking the pedestrian's foot location based on data from AHRS and dead reckoning is
441 presented in sections 3.1 and 3.2. A novel algorithm is proposed in section 3.3 which allows oGRF to be
442 estimated from the same data, based on some simple assumptions.

443 **3.1   Pedestrian tracking algorithm (dead reckoning)**

444 Pedestrian dead reckoning (PDR) is a generic term describing relative (i.e. to a known reference)
445 navigation techniques used to determine the position and orientation of a walker [38]. The input data for
446 PDR usually comes from MEMS-based monitors attached to human body. Different methods of
447 implementation of PDR are discussed elsewhere, e.g. [38]. The PDR algorithm used in this study was
448 previously adopted in [39] and in principle relies on double integration of acceleration data from a
449 monitor attached to a foot. The obtained translational motion is combined with orientation estimates from
450 AHRS gyroscopes and magnetometers that allow the direction of heading to be determined. The
451 arrangement of the AHRS used for PDR is shown in Figure 9 together with its LCS.

452
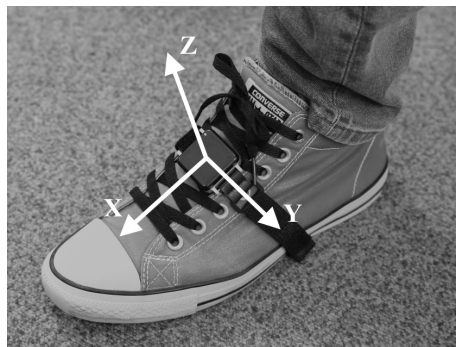
453 Figure 9 AHRS attached to a foot, used for PDR. Three axes of LCS are denoted in white.

454 It is well known that numerical integration of noisy acceleration signals introduces drift. To reduce this
455 effect the PDR algorithm exploits the bipedal nature of human gait. The gait cycle comprises two

456 distinctive periods in which the leg is either in contact with the ground (i.e. stance phase) or swinging (i.e.

457 swing phase). During stance phase the foot rolls from the heel to the toes, but there is a period during

458 which it can be considered stationary. Identifying these periods allows zero-velocity updates (ZUPTs) to

459 be applied which greatly improve the accuracy of estimates of translational foot motion [40].

460 The ZUPT starts with threshold detection in the acceleration magnitude:

461
$$|a| = \sqrt{a_{X,LCS}^2 + a_{Y,LCS}^2 + a_{Z,LCS}^2} \qquad (5)$$

462 below which the foot can be considered stationary, where the acceleration magnitude is previously

463 relieved of the component due to gravitational acceleration. Although, in general, zero acceleration is not

464 a sufficient condition for detecting zero velocity periods, it is reasonable to assume this relationship to

465 hold for foot motion in walking. This can be understood from Figure 10 (a), containing raw acceleration

466 output in LCS of a foot monitor (see Figure 9) collected during a walking trial. The regions of constant

467 (i.e. near zero) velocity are where the curves are flat and, after subtracting gravitational components,

468 converge. This differs from a non-stationary period in foot motion, dominated by a leg swing, when the

469 rate of change of acceleration is relatively high. Figure 10 (b) shows the corresponding acceleration

470 magnitude data obtained with Eq. (5), treated with two-way second-order Butterworth low-pass filter with

471 cut-off frequency 4.5 Hz. The beginnings and end of the identified non-stationary periods of foot motion,

472 based on the threshold of 0.8 ms^{-2}, are denoted by circles and dots, respectively.
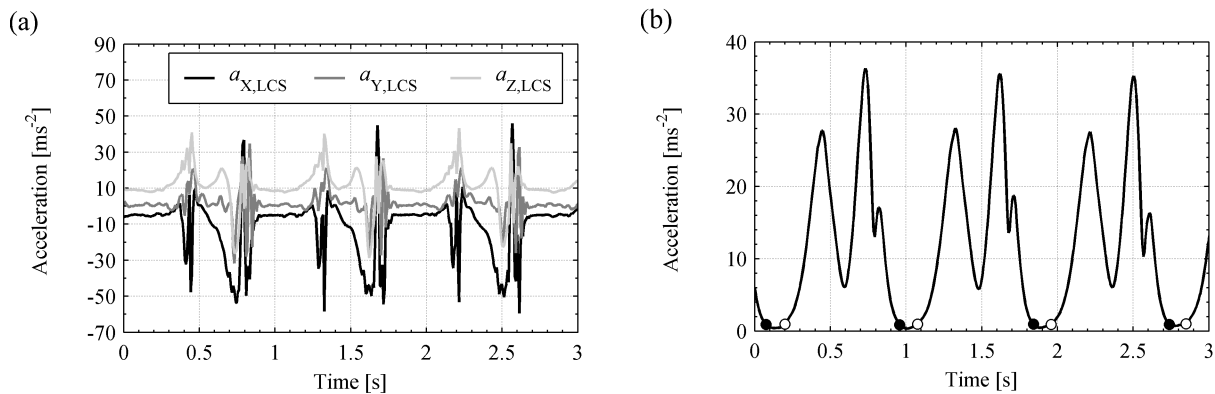
473 Figure 10 (a) Raw acceleration signals in LCS measured during a walking trial. (b) Implementation of the

474 threshold detection on acceleration magnitude data. Start and end of each non-stationary

475 period in foot motion are marked by circle then dot.

476 The raw monitor acceleration data in LCS are resolved to WCS with help of quaternions, then each

477 acceleration signal is numerically integrated using the finite difference (mid-point) method and the values

478 of velocity during the stationary period in foot motion are reset to zero. For each identified non-stationary

479 period of foot motion a linear trend is next subtracted from the calculated velocity vector. This trend is

480 constructed between a pair of data points in that vector corresponding to consecutive instances at which

481   the foot motion is initiated and terminated, as can be seen in Figure 10 (b). Note these points are not

482   equivalent to instances of stance phase and swing phase termination. Exemplar results of application of

483   ZUPTs are presented in Figure 11. The orientations of monitors in WCS are expressed relative to a North,

484   West and vertical global reference frame and a velocity for each direction is calculated and presented in

485   the plots from the top to the bottom, respectively. The drift in the velocity signals is visible in Figure 11

486   (a) containing data obtained by single integration of recorded acceleration signals. Figure 11 (b) shows

487   the same data but obtained after applying ZUPTs. The difference between data in Figure 11 (a) and (b) is

488   caused by errors accumulated due to drift after approximately 30 seconds of walking.
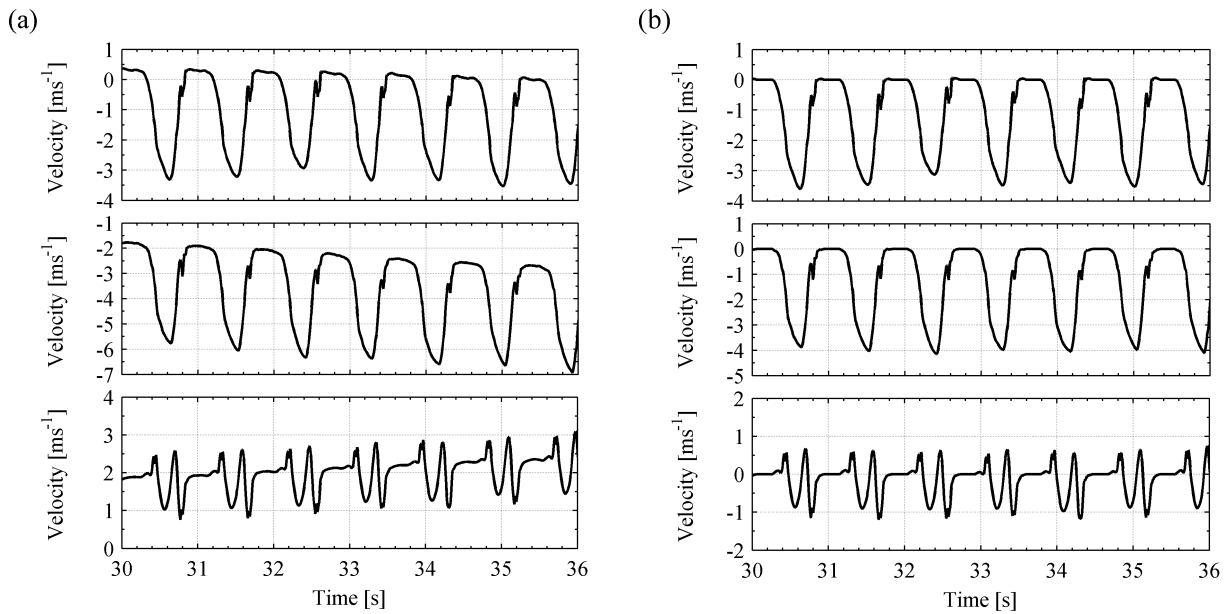
489   Figure 11 Correction of drift in velocity signals using ZUPT. (a) Velocity signals obtained by integration

490   of acceleration data. (b) Velocity signals corrected for drift. For (a) and (b) the two top plots

491   correspond to North and West horizontal directions in WCS while the bottom plot

492   corresponds to the vertical direction.

493   Having performed ZUPTs, the velocity signals are integrated once more to obtain foot displacement in

494   WCS. An exemplar outcome of this procedure is presented in Figure 12. The data come from a test during

495   which a subject was asked to walk between two lines drawn 30 m apart. The top plot shows the horizontal

496   displacement of the instrumented foot relative to North and West. The subject was heading South-East in

497   a fairly straight line. The middle plot shows vertical foot motion against the magnitude of horizontal

498   displacement obtained by taking a square root of the sum of squares of data in the top plot, referred to as

499   the distance travelled. The subject descended by approximately 0.35 m, corresponding to the average

500   downward slope of the walking surface slope of 0.6 degrees. The bottom plot shows the magnitude of

501   horizontal displacement against time. The distance of 30 m travelled by the walker is recovered with very

502   good accuracy. The tangent to the average slope of the signal represents the walking velocity, which is

503   approximately 1.5 ms^{-1}. The wavelike pattern of the signal composed of flat and inclined parts is a

504   resultant of periods in which the foot is in contact with the ground and swinging, respectively.
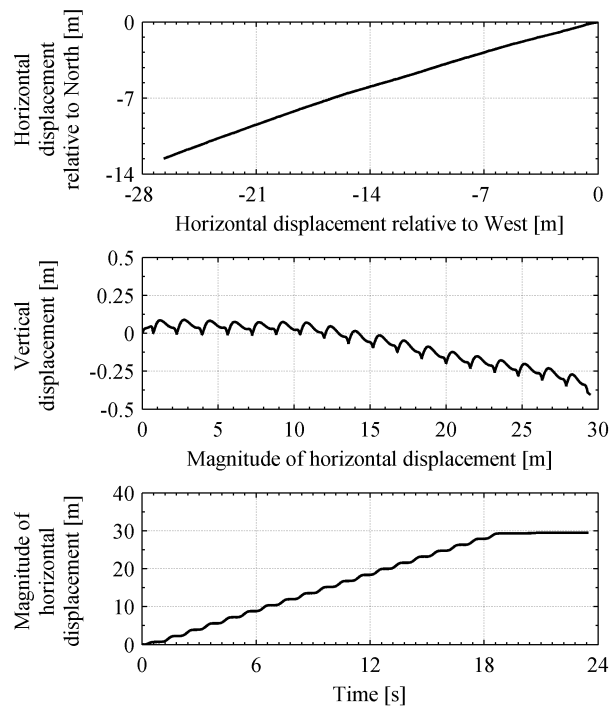
505   Figure 12 Exemplar translational data of foot motion obtained with PDR.

506   **3.2**   **PDR calibration and heuristic drift correction**

507   Section 3.1 mentioned the importance to PDR of calibrating the acceleration magnitude threshold below

508   which the foot can be considered stationary. The difficulty arises since the obtained acceleration

509   amplitudes are affected by variations in monitor placement (in repeated deployment), the type of footwear

510   worn, difference in foot motion patterns between individuals, etc. Therefore, rather than assigning one

511   value and assuming its universal applicability, the threshold needs to be adjusted separately for each

512   individual. In the case of a footbridge, having a clear direction of travel (including any gradient), walking

513   a fixed distance provides a means to calibrate the threshold.

514   The algorithm only accounts for the lower harmonic components of motion because data from the

515   monitored foot are low-pass filtered during PDR. Nevertheless, this feature does not compromise

516   capability to capture real pedestrian behaviour since the spatio-temporal variability of motion patterns is

517   preserved. Another important feature of the algorithm is that the direction of travel of the uninstrumented

518   foot is implicitly assumed to be consistent with the longitudinal axis of the bridge. This is because it is the

519   magnitude of horizontal foot displacement (e.g. shown at the bottom plot in Figure 12) which is used for

520   determining pedestrian location on the bridge. Any deviation of a pedestrian from a perfect straight, e.g.

521   due to veering (see [9] for discussion of this), could reasonably be taken as random so as to increase

522 actual distance travelled approximately evenly along the path. In this case a simple correction can be
523 applied using the known straight line distance.

3.3 Determination of the origin of ground reaction force vector (oGRF)

525 Determining the precise location of oGRF typically requires either a force plate, appropriately arranged
526 instrumented treadmill, instrumented insoles, pressure mats or shoes instrumented with force cells. Only
527 the latter two methods offer capabilities of identifying oGRF in normal overground walking over long
528 distances. However, even data collected using the latter two methods, if used alone, are not fit for purpose
529 since the obtained oGRF is expressed relative to the position of the foot, whose coordinates relative to the
530 structure are unknown. Therefore in this study, to keep the instrumentation simple, a novel algorithm for
531 the determination of approximate (i.e. pseudo) location of oGRF was developed in which output of PDR
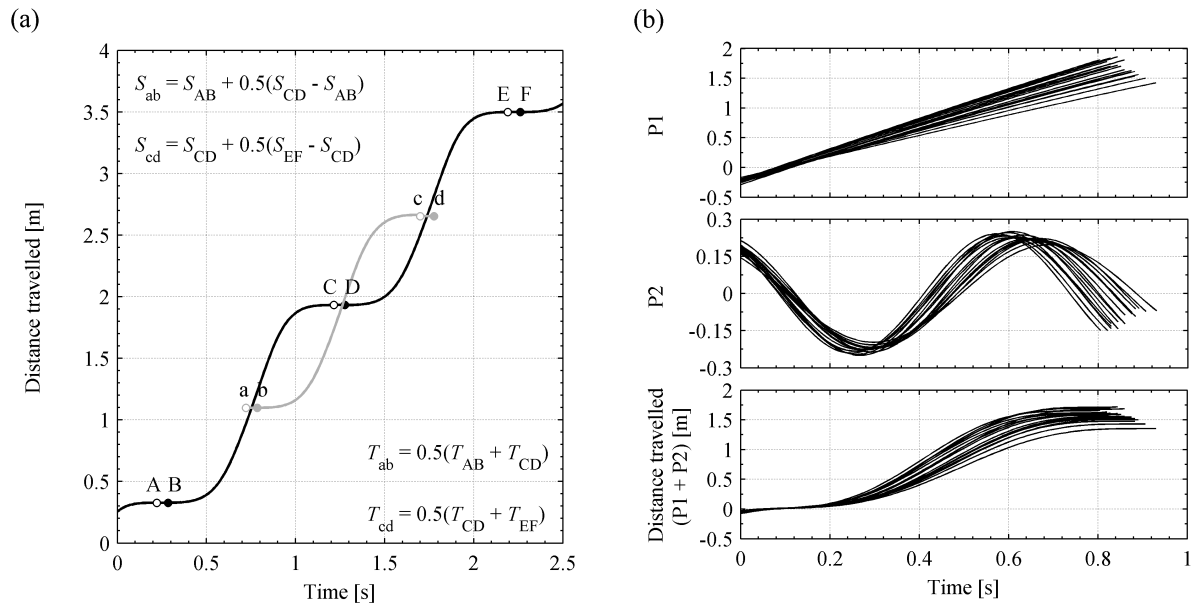532 is used as an input.

533 As with PDR, the main idea behind the oGRF identification algorithm derives from the bipedal nature of
534 human gait. During a single support phase, oGRF is located within the boundaries of the foot in contact
535 with the ground. During a double support, when body weight shifts to the contralateral (i.e. stepping) leg,
536 oGRF travels to the location of the foot of that stepping leg.

537 Algorithm implementation requires information on the motion of both feet. Putting one monitor on each
538 foot would satisfy this requirement, however, this would require three monitors per pedestrian, i.e. one to
539 estimate the force and one monitor on each foot (the tasks described in sections 3.3.1 and 3.3.2 can then
540 be skipped). In the situation where the number of monitors is limited, one-third reduction in
541 instrumentation can be achieved by instrumenting one foot only, thus allowing larger pedestrian groups to
542 be studied. To that end, a three-stage method allowing the motion of the uninstrumented foot to be
543 synthesised is presented and its performance is analysed. The first stage (section 3.3.1) determines
544 positions and locations where the uninstrumented foot can be considered stationary (i.e. flat on the
545 ground) and the second stage (section 3.3.2) determines trajectories of the uninstrumented foot during
546 non-stationary periods. To ensure smooth transition between stationary and nonstationary periods, section
547 3.3.3 stitches the patterns together to produce a smooth continuous motion pattern (trajectory). The
548 reconstruction process was checked using data obtained with both feet instrumented with AHRS, by
549 reconstructing the motion of one foot based on data from the other foot and yielded satisfactory results.
550 Once the information on the motion of both feet is available, double support phases of gait can be
551 identified, allowing oGRF tracking in time and space (section 3.3.4).

3.3.1 Stationary periods in uninstrumented foot motion

553 Positions where the uninstrumented foot is stationary are effectively estimated by assuming they are
554 equidistant between successive stationary locations of the instrumented foot obtained by PDR, as

indicated in Figure 13 (a). The black curve in Figure 13 (a) shows the distance travelled by the

556 instrumented foot, taken as the magnitude of horizontal foot displacement obtained with PDR (see section

557 3.2), plotted with respect to time.

(a)

$$S_{ab} = S_{AB} + 0.5(S_{CD} - S_{AB})$$

$$S_{cd} = S_{CD} + 0.5(S_{EF} - S_{CD})$$

$$T_{ab} = 0.5(T_{AB} + T_{CD})$$

$$T_{cd} = 0.5(T_{CD} + T_{EF})$$

(b)

Figure 13 (a) Reconstruction of stationary periods in the uninstrumented foot motion. The measured

559 position of the instrumented foot is denoted by a black curve. The segments AB, CD and EF

560 are the identified plateaus in instrumented foot data. The segments ab and cd denoted in grey

561 are the reconstructed plateaus for the uninstrumented foot. Formulae for spatial location (S)

562 and duration (T) of those segments are given on the plot. For all data, circles and dots mark

563 the beginnings and ends of plateaus, respectively. The grey curve describes the motion of the

564 uninstrumented foot during non-stationary period. (b) Exemplar performance of fitting Eq.

565 (6) for non-stationary periods of the instrumented foot motion.

566 The plateaus evident in the plot, denoted by segments AB, CD and EF with circles and dots marking their

567 beginnings and ends, respectively, are when the instrumented foot is stationary. The midpoints between

568 the plateaus are then identified, which split the distance travelled during a step into two equal lengths. For

569 example, the midpoint in distance travelled during a step in which the foot moved from AB to CD is

570 denoted by ab. The modulus of the difference between the ordinates (distance) of two consecutive

571 midpoints (e.g. ab to cd) is assumed to be the distance travelled by the uninstrumented foot during a step.

572 Durations of plateaus for uninstrumented foot are taken as the average of the durations of the two plateaus

573 immediately surrounding the associated midpoints for the instrumented foot. The plateaus corresponding

574 to the uninstrumented foot are assumed to occur at times such that abscissas (timing) of their midpoints

575 fall at the corresponding abscissas of midpoints of the non-stationary periods of instrumented foot data.

576 The equations describing the location of midpoints (S) and their durations (T) are given in Figure 13.

3.3.2 Non-stationary periods in uninstrumented foot motion

Reconstruction of the non-stationary period of the uninstrumented foot motion (e.g. segment bc in Figure 13 (a)) is based on finding a suitable fit $k(t)$ to the trajectory of the non-stationary period of the instrumented foot motion (e.g. segments BC and DE in Figure 13 (a)). A suitable form for $k(t)$ is the sum of two sinusoidal components:

$$k(t) = \underbrace{\alpha_1 \sin(\alpha_2 t + \alpha_3)}_{P1} + \underbrace{\beta_1 \sin(\beta_2 t + \beta_3)}_{P2} \tag{6}$$

where α_1, α_2, α_3, β_1, β_2 and β_3 are coefficients to be determined. The parts of the function characterised by slow and fast oscillation, referred to as P1 and P2 respectively, reflect the horizontal progression of the foot and its swinging motion. This can be seen in Figure 13 (b) presenting fitted data for non-stationary periods of the instrumented foot for a subject with $m_p = 81\,\text{kg}$ and $h = 1.83\,\text{m}$ walking the distance of 30 m at variable speed, i.e. purposely increasing and decreasing their velocity to provide a test of the algorithm. For the record of which a truncated time history is shown in Figure 13 (a), the goodness of fit statistics expressed in terms of the average adjusted R-square and standard error, based on fitting to 72 steps collected during a single trial, are 0.999 and 0.005 m, respectively. Similar goodness of fit statistics were obtained for all other analysed data regardless of the speed of travel of the walker and their pacing frequency.

Having shown that the function in Eq. (6) provides a good estimation of the motion of the instrumented foot, the next step is to apply this to reconstruct corresponding non-stationary period of uninstrumented foot motion. To this end the coefficients of P1 and P2 (i.e. α_1, α_2, α_3, β_1, β_2 and β_3) need to be known a priori. Therefore tests were conducted in which seven people walked a known distance at different speeds with AHRS monitors attached to their feet. The dependence of the coefficients of Eq. (6) on the duration of and distance travelled during non-stationary periods in foot motion was investigated. An example is presented in Figure 14, showing data from a single test during which a subject was asked to walk with a variable speed over the distance of 150 m. The best second-order polynomial surface fits to the data are denoted in grey. The amplitude β_1 and angular frequencies α_2 & β_2 show a strong dependence on duration and distance with adjusted R-square values typically above 0.92 and standard errors for these coefficients below 0.06, 0.005 rad/s and 0.15 rad/s, respectively. Figure 14 shows lower accuracy for fitting amplitude α_1 and invariance of phase angle α_3 & β_3. The low variability of these coefficients relative to the range of phase angle indicates that their mean values can be taken as applicable generally for the tested subject. This observation is substantiated by data in Figure 13 (b) showing that the patterns of evolution of two sinusoidal components of Eq. (6) (P1 and P2) are similar for all fits, although the duration and distance travelled might vary.
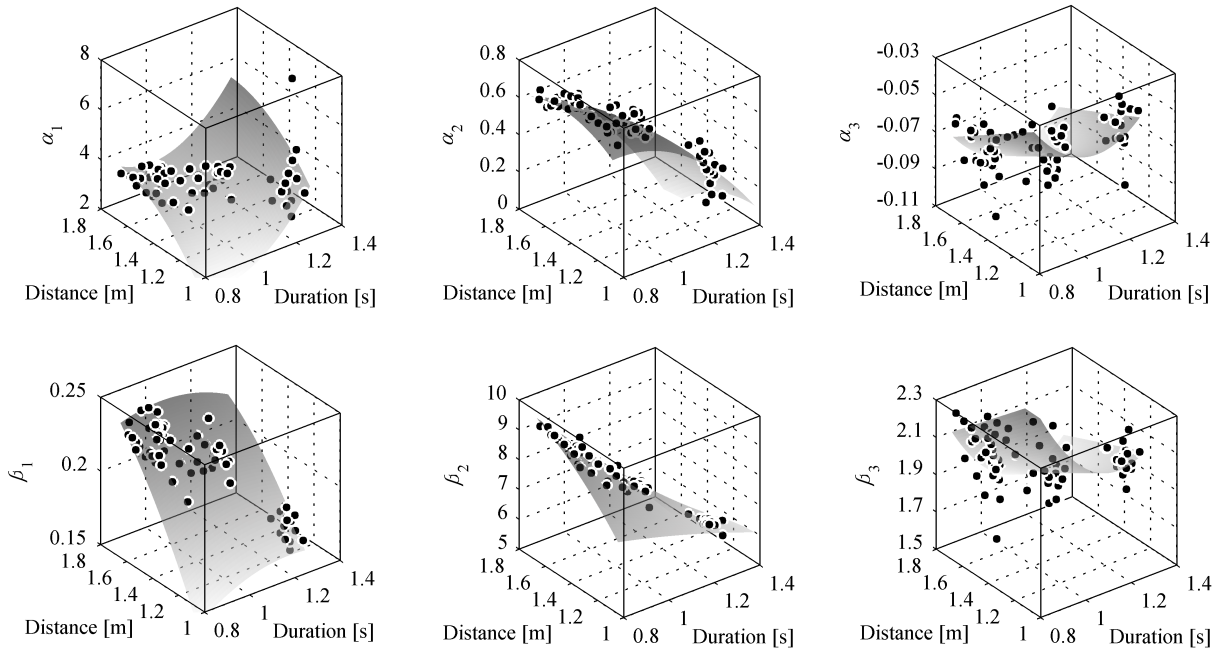
Figure 14 Exemplar coefficients of the fit described by Eq. (6) based on data from one foot derived for a subject with $m_p = 81\,\text{kg}$ and $h = 1.83\,\text{m}$ walking the distance of 150 m at variable speed. The best polynomial surface fit is shown for each coefficient.

Analyses of data collected during a series of tests have shown that the coefficients of Eq. (6) should be calibrated for each subject separately because of inter-subject variability of foot motion pattern and monitor placement (see section 3.2). However, reconstruction of a foot motion pattern based on coefficients drawn from polynomial fits, even if derived separately for each subject, is prone to inaccuracies as the mutual dependence of these coefficients is unlikely to be captured perfectly. Therefore, two additional steps implemented in the algorithm to correct for this effect are described in the next section.

3.3.3 Stitching together time histories for stationary and non-stationary trajectory components for uninstrumented foot

Now having identified constructed time history components corresponding to moving and stationary uninstrumented foot, two minor additional steps (which a busy reader could skip) are needed to arrive at a kinematically correct complete time history of uninstrumented foot motion. The first step adjusts the shape at the ends of a trajectory component for the foot moving, so as to ensure smooth landing at zero velocity. The second step uniformly scales (in distance axis) the trajectory to correct for small discontinuities in position resulting from the first step.
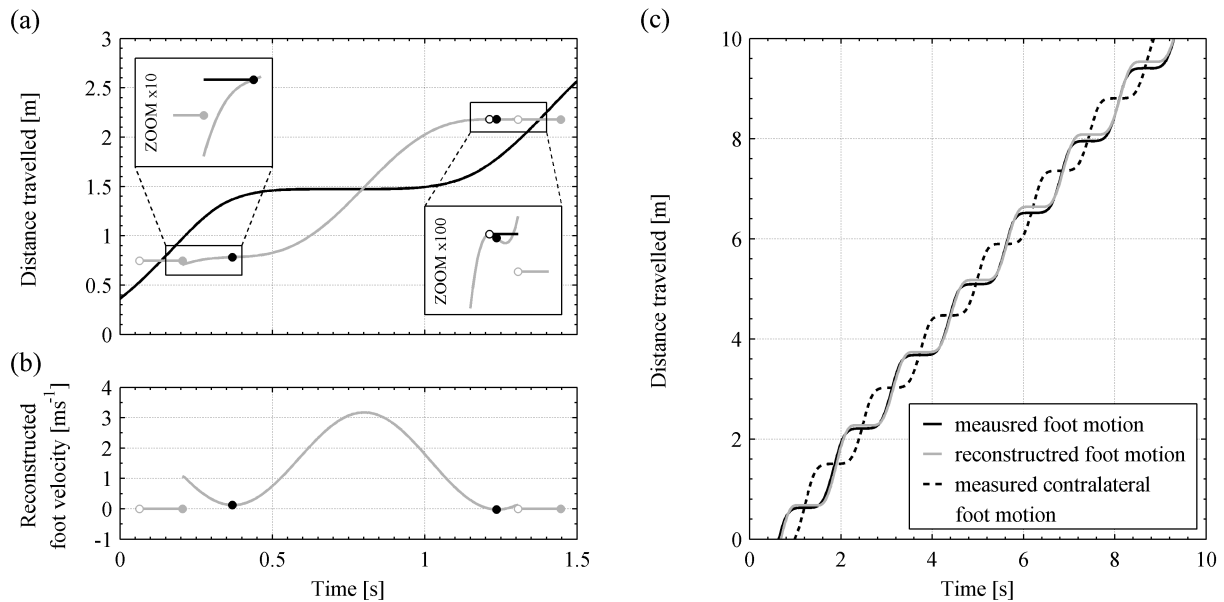
Figure 15 (a) Motion patterns measured on instrumented foot (black curves) and reconstructed for uninstrumented foot (grey curves). (b) The first derivative of the reconstructed pattern of uninstrumented foot motion in (a). Black dots marking local minima in (b) correspond to points of inflection in uninstrumented foot data in (a). Grey circles and dots in (a) and (b) mark the beginnings and ends of the plateaus representing stationary periods in foot motion. Black circles in (a) correspond to the local maximum in reconstructed foot motion. Black lines on zoomed-in subplots in (a) represent linearised ends in the reconstructed motion pattern. (c) Comparison of measured and reconstructed of foot motion.

The nature of the fitted function for the moving foot trajectory does not guarantee monotonic increase where it meets the (level) plateau representing the stationary foot. Points of inflection in the reconstructed (moving) foot trajectory are identified via local minima in the first derivative (velocity, which should be zero). Figure 15 is an example where the points of inflection of the reconstructed (grey) curve in Figure 15 (a) are identified by black dots at 0.37 seconds and 1.24 seconds via the first derivative (velocity) shown in Figure 15(b). Zooming on Figure 15 (a) shows the fitted trajectory to have a turning point just before the point of inflection at 1.24 seconds. After this point (marked as a black dot) the fit suggests that the foot moves backward. To correct for this, the reconstructed foot motion pattern is simply linearised at the ends. This is performed for the range of data from the most inward points defined either by points of inflection or, if they exist (such as on the plot in Figure 15 (a)), local minimum or maximum outwards such that the ends are flat (black lines in the insets of Figure 15 (a)).

The inserts in Figure 15 (a) show that the ends of the corrected patterns (black lines) are displaced with respect to the (stationary) plateaus (grey lines). Therefore in the second step the distance travelled during the reconstructed motion pattern is scaled up or down, stretching or compressing motion pattern in space (rather than time), after which the pattern is realigned between the corresponding plateaus.

650   The accuracy of the described procedures can be inspected in Figure 15 (c). To create this figure an

651   experiment was conducted where monitors were placed on both feet of the pedestrian. The solid black

652   curve shows the measured foot motion (in this case the right foot) and the dashed black curve shows the

653   measured contralateral (left) foot motion. The solid grey curve shows the reconstructed motion of the

654   right foot based on the observed motion of the contralateral (left) foot and the approach presented in

655   sections 3.3.1 – 3.3.3. Figure 15 (c) shows that, broadly speaking, there is a good match between the

656   measured foot motion and the reconstructed foot motion. The Pearson's linear correlation coefficient,

657   calculated after detrending each signal with its linear fit, is 0.97. The lowest values of this coefficient (but

658   still above 0.95) were obtained for tests in which the subjects were asked to walk with variable speed, i.e.

659   deliberately increasing and decreasing their velocity.

660   **3.3.4   Determination of the double support phase of gait and oGRF**

661   The next step in the proposed algorithm determinaes double support phases of gait within the analysed

662   data. Since this information cannot be obtained directly using AHRS, a suitable method was developed

663   using the data from the treadmill experiments to establish a relationship between the walking frequency

664   and duration of double support phase of gait. Stride durations, taken between two consecutive TOs of the

665   same leg, were quantified after discarding the range of data associated with gait inception and termination

666   stages. The durations of two double-support phases of gait occurring within each of those strides were

667   then calculated. The relationship between the percentage duration of double support phase, expressed in

668   relation to stride duration, and pacing frequency is presented in Figure 16. The data are based on averages

669   from strides marked by TOs of right and left legs.
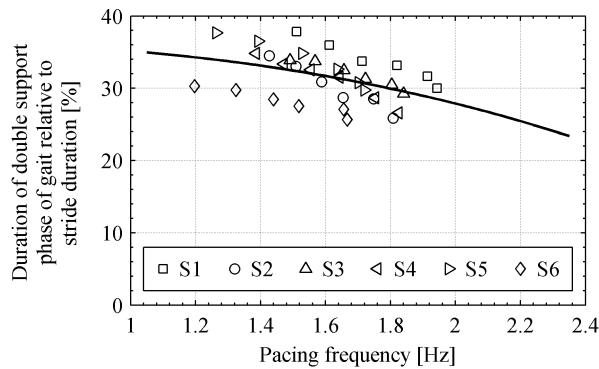
670   Figure 16 Percentage duration of double support phase of gait, expressed in relation to stride duration,

671   against pacing frequency. The trend in data described by Eq. (7) is shown as a black curve.

672   As in the case of the percentage error in Fourier force amplitude corresponding to the pacing frequency

673   presented in Figures 6 and 7, subject specific trends can be seen in data in Figure 16. In order to show the

674   average trend in all data for all subjects, a fit based on power law relationship was calculated:

675                             $$T_{DS} = -0.015 f_p^{2.571} + 0.366 \qquad\qquad (7)$$

676   where T_{DS} is expressed as a percentage of stride duration.

677   It is reasonable to assume that the double support phase of gait occurs periodically when the two feet are

678   the furthest apart. After identifying these points in foot motion data, stride durations corresponding to

679   these points are established by taking the period between the ends of two plateaus in instrumented foot

680   motion containing considered double-supports. A reciprocal of stride duration is assumed to be equal to

681   the instantaneous stride frequency, which is half the pacing rate. Having established the instantaneous

682   pacing rate, the duration of the double support phase of gait is calculated from Eq. (7). Double supports

683   are assumed to occur symmetrically around the identified points where the feet are the furthest distance

684   apart. Exemplar performance of the proposed algorithm for determining oGRF is presented in Figure 17.

685   The regions corresponding to double support phase of gait are shaded in grey and the evolution of the

686   location of oGRF is shown as a thick black curve. The curvature of foot motion patterns during double

687   support periods is associated with progression of a foot during roll-over.
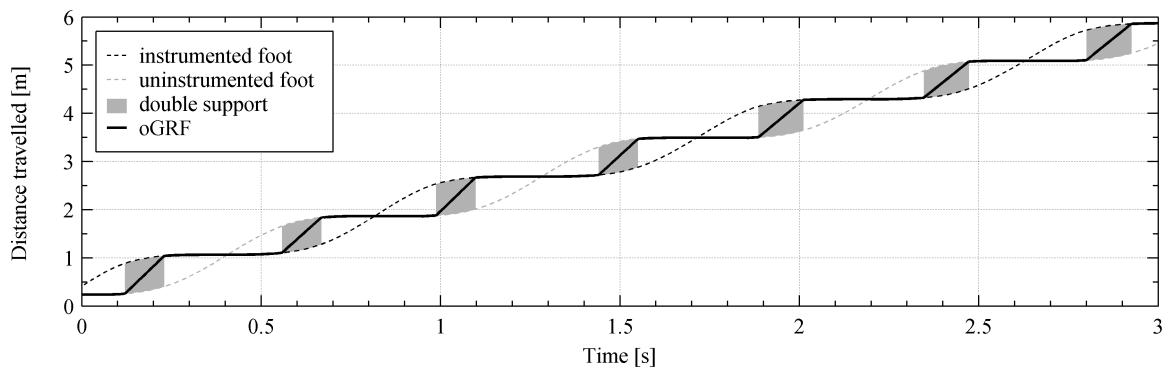

688   Figure 17 Exemplar performance of the proposed algorithm for the determination of the origin of ground

689   reaction force vector.

690   The performance of the proposed pedestrian force location tracking method will be further discussed in

691   section 5, reporting results of a study performed to show the applicability of the proposed framework. The

692   experimental campaign used to gather data on pedestrian and bridge behavior is described next.

693   **4   In-situ testing on a full-scale structure**

694   Controlled pedestrian loading tests were performed on Baker Bridge (BB) in Exeter, UK. BB was

695   constructed in 2008 and is located close to the Sandy Park Stadium (50°42'38.6"N 3°28'13.3"W) which is

696   the home ground of the Exeter Chiefs rugby team. The bridge (see Figure 18) crosses a dual carriageway

697   and has total length approximately 108.6 m with main span (South end) and back span (North end) having

698   approximate lengths of 71.285 m and 37.36 m, respectively. The 42 m high steel A-frame tower supports

699   the ladder deck via six pairs of cable stays with another pair of cable stays anchored at the North

700 abutment. The deck has two continuous longitudinal steel main beams pinned at the North abutment,
701 resting on a tower crossbeam via pad bearings and having a sliding expansion joint at the South abutment.

(a)

(b)

(c)

(d)
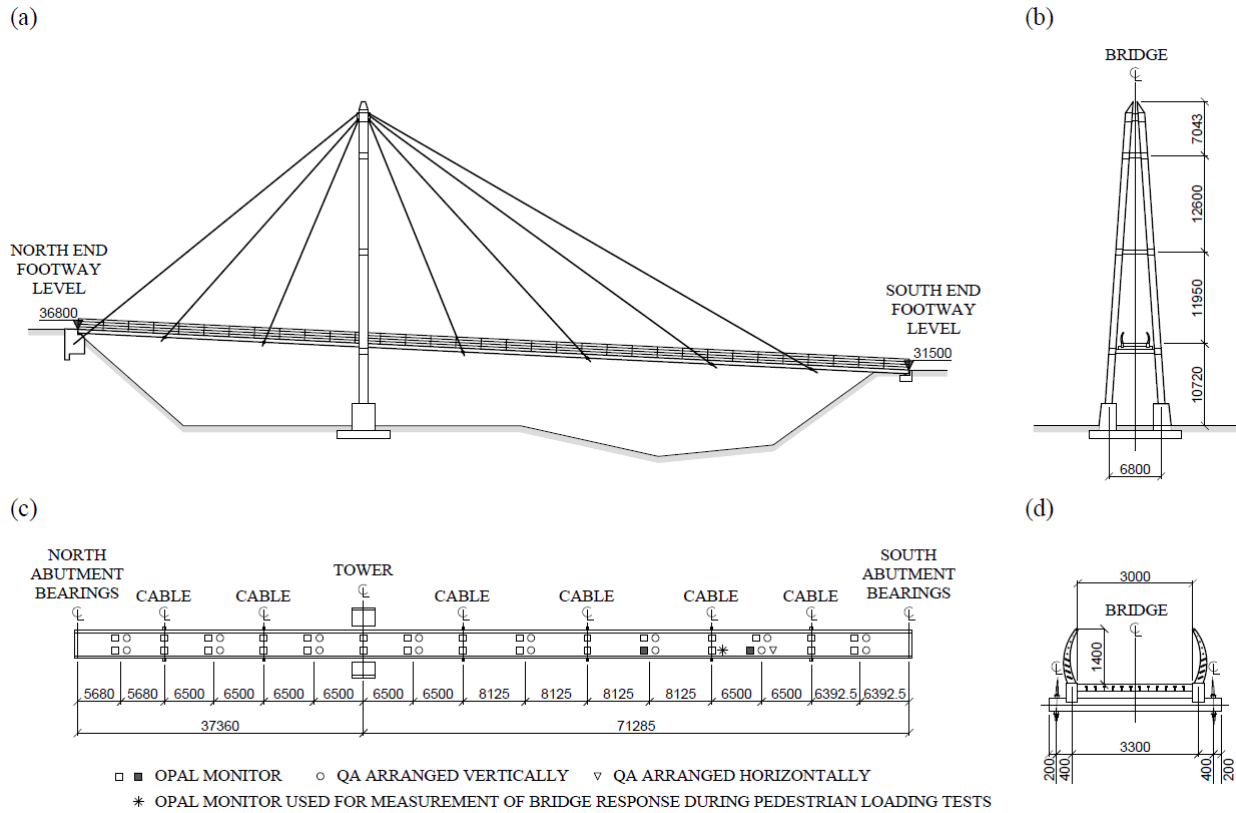
702 Figure 18 (a) Elevation and (b) cross-section through the tower of Baker Bridge. (c) The true plan on
703 deck together with instrumentation layout. The roving and reference Opal^{TM} monitors are
704 denoted by empty and filled squares, respectively. (d) A cross-section through the deck.

705 BB deck is at least 10 m above the ground throughout most of its span and has a downward North-to-
706 South slope of approximately 2.79 degrees, causing 5.3 m difference in the footway levels at the ends of
707 the bridge. The footway is a 3 m wide concrete slab enclosed by 1.4 m high steel parapets. An estimated
708 total 49 tonnes of steel and 98 tonnes of concrete were used in the deck construction.

709 A dedicated modal testing campaign conducted to obtain modal properties of the empty bridge is
710 described in the next section.

711 **4.1 Modal testing**

712 Two instrumentation systems were deployed in order to determine BB modal parameters i.e. natural
713 frequencies, damping ratios and mode shapes. These were a set of six Opal^{TM} monitors and an array of
714 conventional wired Honeywell QA quartz-flex low noise servo-accelerometers used to cross-check the
715 more noisy data from the Opal^{TM} AHRS monitors. One QA (see Figure 18 (c)) was set horizontally to
716 check for coupled cross-axes modes. The ambient vibration testing performed with AHRS used a standard

717 method of allocating reference and roving accelerometers. The method is the same as used on Humber
718 Bridge [41], and provided the definitive set of BB mode shapes, shown in Figure 19.

719 Parameter estimates obtained from ambient testing are known to exhibit significant variance [42], so
720 specific and more reliable parameter values appropriate to the level of response due to a pedestrian were
721 obtained by further measurements using a force plate and an instrumented hammer. The force plate was
722 used to record vertical forces during short sequences of up to eight jumps prompted by a metronome set
723 to a bridge natural frequency estimated in the ambient tests. The free decay of response to jumping was
724 used to extract accurate damping and frequency values via curve fitting to exponentially decaying
725 sinusoids [43].

726 Additionally, single degree of freedom circle fitting to the frequency response function of acceleration to
727 force derived from jumping tests was used to estimate modal masses, using hammer testing to cross-
728 check values. Modal mass values are based on mode shapes having maximum vertical mode shape
729 ordinate set to unity, and are applicable for loads applied at any point of the deck for modes 1-4 and along
730 the walkway edge for mode 5.

731 The modal parameter values appropriate for response calculations are given in Table 3. The inherent
732 damping ratios for all the presented modes are relatively low [44].
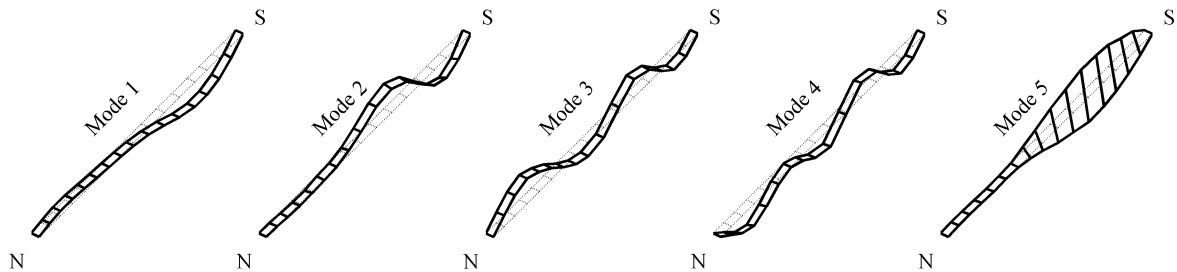
733 Figure 19 The first five lowest identified mode shapes of Baker Bridge. North and South ends of the
734   bridge are denoted by N and S, respectively.

735 Table 3 Modal properties of Baker Bridge for the first four lowest vertical modes and the first torsional
736   mode.

	Mode 1	Mode 2	Mode 3	Mode 4	Mode 5
Frequency, f_n [Hz]	0.94	1.61	2.00	2.24	2.84
Modal mass, M_n [tonne]	55	68.4	57.2	57.3	40
Damping ratio, ζ_n [%]	0.16	0.19	0.32	0.37	0.22

737

738 Mode 2 and 3 frequencies correspond to pacing rates which can be expected in the case of relaxed

739 walking e.g. for a crowd on a match day, and the case of normal walking, respectively. Therefore, the

740 controlled pedestrian loading tests focused on the behaviour of BB at frequencies of these two modes.

741 **4.2   Controlled pedestrian loading tests**

742 To assess the loading model introduced in section 2 and the algorithm for the pedestrian force location

743 tracking introduced in section 3, a series of tests with a single walker was performed on BB. Monitors

744 were attached at the sternum, navel, lower back, C7 and one foot. The test subject (a 34 years old male,

745 $m_p = 81\text{kg}$ and $h = 1.83\text{m}$) was asked to walk to the rhythm of a metronome set to 1.6 or 2 beats per

746 second, corresponding to the frequencies of mode 2 and 3, respectively (see Table 3). Each test started

747 from the subject standing still at a line marked 1 m behind the bridge end (i.e. outside of the boundary of

748 the deck). The subject was asked to terminate gait 1 m behind the other end of the bridge, at a marked

749 line. This allowed the duration of and the distance travelled (110.6 m) during a test to be easily identified

750 in the AHRS data. Two tests were performed at each metronome rate in which the pedestrian walked

751 either from North to South or from South to North across the bridge. This was to investigate if the slope

752 of the bridge has any effect on the results. The response of the bridge to the walker was measured by the

753 monitor placed at the location denoted in Figure 19 (c) by a star. The results of the controlled pedestrian

754 loading tests are reported in the next section, comparing the measured bridge response and the response

755 simulated using the proposed framework.

756 **5   A study comparing measured and simulated bridge response**

757 Having introduced the procedures leading to reconstruction of pedestrian force (section 2) and its

758 instantaneous location (section 3), this section examines how successful these procedures are at

759 simulating footbridge response. A modal model of BB is built using information from section 4.1, to

760 which pedestrian force is applied. The location of this force is taken either as moving at a constant speed

761 along the bridge or equal to oGRF (see section 3.3).

762 The flowchart in Figure 20 presents a graphical summary of the proposed framework. The last and

763 standard step, represented in the lower right of the figure, is calculating bridge response to moving and

764 mode-shape modulated pedestrian force. The following equation of motion can be written for each mode:

765
$$X(t) + 2\zeta_n \omega_n X(t) + \omega_n^2 X(t) = \frac{1}{M_n} \sum_{i=1}^{N} F_i(t, x_i) \phi_{i,n}(x_i) \tag{8}$$

766 where X is the modal displacement, ζ_n is the damping ratio, ω_n is the natural frequency, M_n is the

767 modal mass, F_i is the force amplitude of the $i-\text{th}$ pedestrian, N is the total number of pedestrians on

768　the bridge, $\phi_{i,n}$ is the amplitude of the n-th mode shape at $i-$th pedestrian location, x_i is the $i-$th

769　pedestrian location, and dots over symbols represent relative differentiation with respect to time t.
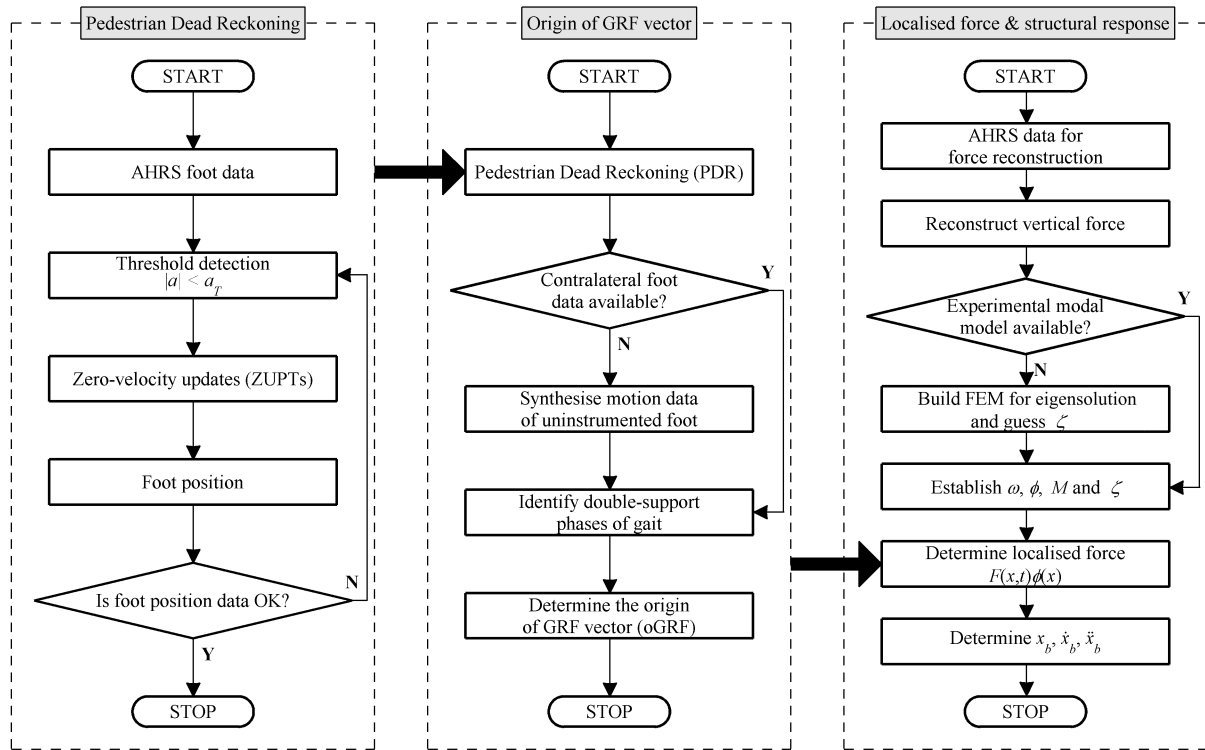
770　Figure 20 A flowchart showing the proposed framework for the determination of localised pedestrian

771　forces on full-scale structures using attitude and heading reference systems.

## 5.1 Response of the bridge to a single pedestrian

773　In this section the measured response of the bridge subjected to loading from a single walking pedestrian

774　is compared to the response predicted by the proposed framework. The simulated and measured vertical

775　responses in mode 2 and mode 3 for the pedestrian walking at 1.6 Hz (chosen to directly excite mode 2)

776　and at 2 Hz (chosen to directly excite mode 3), respectively, are shown in Figures 21 and 22. For each

777　mode, the measured response was band pass filtered with two-way fourth-order Butterworth low-pass

778　filter with cut-off frequencies $f_n \pm 0.1$ Hz. The data in Figures 21 and 22 (a) are from tests in which the

779　pedestrian was walking from the North to the South end of the bridge, and in Figures 21 and 22 (b) from

780　tests in which the pedestrian was walking from the South to the North end of the bridge. The lengths of

781　signals presented in Figures 21 and 22 correspond to the duration of the respective tests. All simulated

782　data presented in Figures 21 and 22 are based on force reconstructed from monitors attached at C7.

(a)

(b)
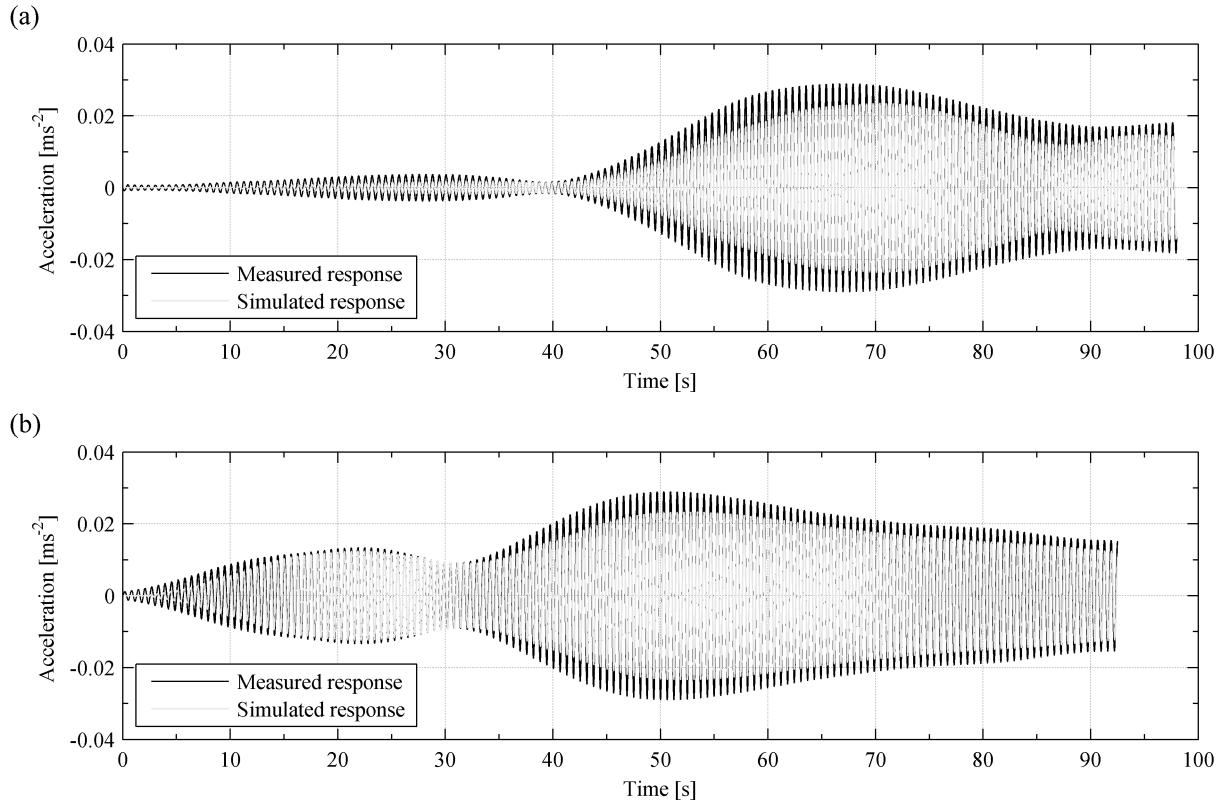
783   Figure 21 Simulated and measured response of Baker Bridge in mode 2 ($f_n = 1.61$ Hz, $\zeta_n = 0.19$ %,

784        $M_n = 68.4 \times 10^3$ kg), for a pedestrian walking at 1.6 Hz (a) from the North to the South end

785   of the bridge, and (b) from the South to the North end of the bridge.

786   The maximum measured acceleration amplitudes in Figures 21 and 22 are just below 0.03 ms^{-2} and 0.2

787   ms^{-2}, respectively. The maximum acceleration amplitudes at the antinodes of mode 2 and mode 3 are 0.05

788   ms^{-2} and 0.37 ms^{-2}, respectively. This shows that the bridge can exhibit lively behavior (i.e. large

789   amplitude response) under the action of walking pedestrians but its response is acceptable according to

790   the guidance at the time of construction [45].

791   Figure 21 shows that the simulated response amplitudes for mode 2 generally underestimate the measured

792   response. A converse relationship can be seen for mode 3 in Figure 22. However, the patterns of

793   evolution of the amplitude of simulated response generally follow the measured data well. The maximum

794   response amplitudes in mode 2 are approximately an order of magnitude lower than in mode 3.

(a)

(b)
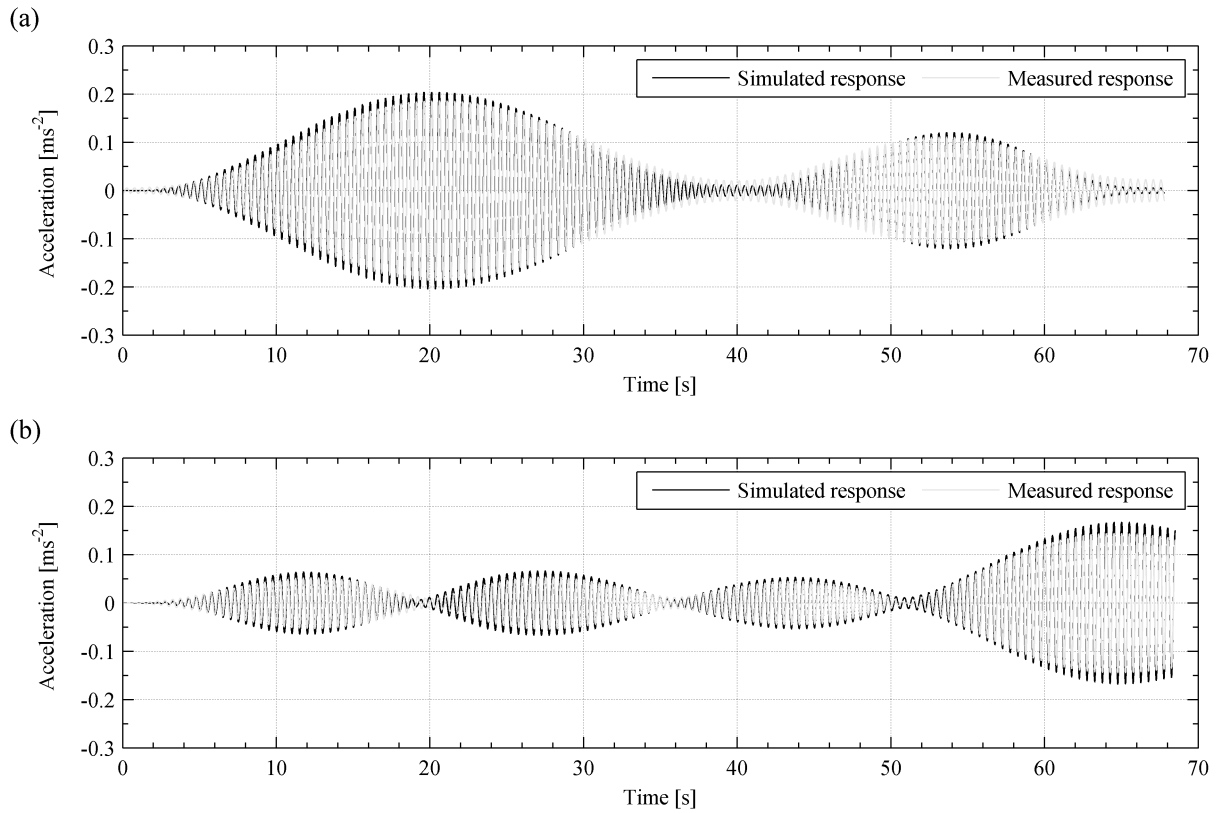
795   Figure 22 Simulated and measured response of Baker Bridge in mode 3 ($f_n = 2\text{Hz}$, $\zeta_n = 0.32$ %,

796          $M_n = 57.2 \times 10^3$ kg), for a pedestrian walking at 2 Hz (a) from the North to the South end of

797   the bridge, and (b) from the South to the North end of the bridge.

798   A detailed comparison between the measured and simulated results based on force reconstructed using

799   AHRS data from different body landmarks is presented in Table 4. Three performance indices are given:

800   percentage difference in maximum acceleration amplitude relative to the measured data, average RMS

801   error in the envelope of acceleration amplitude and Pearson's linear correlation coefficient. The last two

802   indices were calculated after discarding the first 10 s of the signal due to the effect of initial conditions.

803   Normal and italic font styles denote the results obtained by assuming a constant walking speed and using

804   the algorithm for tracking oGRF, respectively. For brevity, the tests with the subject's pacing rate

805   corresponding closely to mode 2 & 3 frequencies are referred to as T1, T2 & T3 and T4, respectively. The

806   direction of travel was from the North to the South end of the bridge for T1 and T3 (i.e. downhill

807   walking) and from the South to the North end of the bridge for T2 and T4 (i.e. uphill walking). The

808   average walking speeds during T1, T2, T3 and T4 were, respectively, 1.13 ms^{-1}, 1.2 ms^{-1}, 1.64 ms^{-1} and

809   1.61 ms^{-1}.

810

811

Table 4 Performance indeces for simulated response of BB for walking tests with a single pedestrian. The results are representative of the pedestrian loading reconstruction procedure based on data from AHRS attached at LB, N, S and C7. Normal and italic font styles denote the results obtained by assuming a constant speed of the walker and using the algorithm for tracking oGRF, respectively.

Performance indices	**T1** mode 2 North → South				**T2** mode 2 South → North				**T3** mode 3 North → South				**T4** mode 3 South → North			
	LB	N	S	C7	LB	N	S	C7	LB	N	S	C7	LB	N	S	C7
Difference in maximum acceleration amplitude [%]	-46.2	-22.8	-36.1	-29.9	-40.4	-24.0	-13.7	-25.7	2.3	11.7	12.8	8.7	10.0	10.5	23.6	13.9
	-59.5	*-32.8*	*-47.7*	*-41.6*	*-58.1*	*-39.3*	*-27.4*	*-41.1*	*-14.9*	*-4.1*	*-2.9*	*-7.6*	*-8.1*	*-7.5*	*8.2*	*-3.4*
Average envelope RMS error [ms^{-2}]	0.0064	0.0045	0.0057	0.0052	0.0024	0.0037	0.0057	0.0039	0.0106	0.0158	0.0170	0.0127	0.0064	0.0070	0.0143	0.0083
	0.0076	*0.0059*	*0.0069*	*0.0065*	*0.0075*	*0.0057*	*0.0044*	*0.0059*	*0.0212*	*0.0130*	*0.0131*	*0.0156*	*0.0036*	*0.0035*	*0.0061*	*0.0030*
Pearson's linear correlation coefficient	0.943	0.990	0.972	0.962	0.966	0.978	0.975	0.965	0.990	0.941	0.989	0.973	0.986	0.968	0.984	0.979
	0.938	*0.985*	*0.964*	*0.955*	*0.953*	*0.972*	*0.967*	*0.953*	*0.988*	*0.937*	*0.988*	*0.971*	*0.989*	*0.974*	*0.987*	*0.984*

A strong linear correlation between the measured and simulated response of the bridge has been found for all cases, with positive values of Pearson's linear correlation coefficients in Table 4 indicating in-phase relationships. Figures 21 and 22 indeed show that the peaks in the measured response and the response simulated based on data from C7, occurring at the intervals equal to reciprocal of the modal frequencies, are aligned in time reasonably well.

5.1.1 Results for T1 and T2 (mode 2)

Examination of differences in maximum acceleration amplitude in Table 4 shows that the simulated data generally underestimate the maximum acceleration amplitudes for T1 and T2. This is the most pronounced for LB, which agrees with the results in Figures 6 and 7 (a) showing that the largest error in the amplitude of the Fourier component of force for $f_p = 1.6\,\mathrm{Hz}$ and $v \in \langle 1.13; 1.2 \rangle\,\mathrm{ms^{-1}}$ can be expected from a model based on data collected from this body landmark. However, while the negative difference in maximum acceleration amplitude is consistent with data presented in section 2 for LB, a positive difference would be more likely for N and S. Interestingly, the simulation results obtained using oGRF are less accurate than those obtained assuming a constant walker speed. The average absolute difference in maximum acceleration amplitude relative to the measured data for all models using oGRF is approximately 43%, compared with 30% obtained from models assuming a constant walker speed. The best accuracy in terms of the maximum response amplitude for T1 and T2 is found for N and S, respectively, which underestimate the measured response by 22.8% and 13.7%. The maximum average RMS envelope error for T1 and T2 is 0.008 ms^{-2} for LB. This value stands at 26% relative to the maximum acceleration amplitudes for T1 and T2, respectively, measured at 0.029 ms^{-2} in both tests.

5.1.2   Results for T3 and T4 (mode 3)

Better performance of the framework is evidenced for T3 and T4. All models assuming a constant walker speed tend to overestimate maximum acceleration amplitudes, which seems to be consistent with data in Figures 6 and 7. The least and greatest differences for both T3 and T4 are found for LB and S, respectively. The simulation results obtained using oGRF improve the match with the maximum measured response, except for LB in case of T3, most often changing sign of the difference, i.e. resulting in underestimated vibration amplitudes. The average absolute difference relative to the measured data for all models using oGRF is approximately 7%, compared with 12% obtained for models assuming a constant walker speed. Best accuracy in terms of the maximum response amplitude for T3 and T4 based on results obtained using oGRF is found for S and C7, respectively, which underestimate the measured response by 2.9% and 3.4%. The maximum average RMS envelope error for T3 and T4 is, respectively, 0.021 ms^{-2} for LB and 0.006 ms^{-2} for S. These values stand at 11.34% and 4.21% relative to the maximum acceleration amplitudes for T1 and T2, respectively, measured at 0.187 ms^{-2} and 0.145 ms^{-2}.

5.2   Discussion

Test results demonstrate the feasibility of the proposed methodology. A satisfactory agreement between simulated and measured responses has been found for all the force models (LB, N, S, C7) and both the force localisation procedures (constant velocity & oGRF). A Pearson's linear correlation coefficient higher than 0.94 was found in all cases, corresponding to a coefficient of determination (R^2) higher than 88%. The magnitudes of error in maximum acceleration amplitude for all tests in mode 2 and 3, averaging over all models with both methods of localisation of point of application of force, were found at 36.6% and 9.4%, respectively. The simulated responses might be affected by several error sources, such as uncertainties with the experimental dynamic model, unconsidered exogenous excitation sources, effects of human-structure interactions, errors in the reconstruction of magnitude and locations of GRF. These effects can cumulate or compensate each other. Broadly speaking, the results of simulations for mode 2 (T1 & T2) are worse than the results of simulations for mode 3 (T3 & T4). Mode 2 parameters were the more difficult to estimate experimentally, which might contribute to errors in the simulated responses for that mode. Nevertheless, the magnitudes of the estimated errors are remarkably good compared with the results of similar tests available in literature.

Previous work by Van Nimmen *et al*. [15] has found that pedestrian force models capturing the effect of variability in timing of the onset of pedestrian footsteps (see section 1.2) outperform loading models based on an assumption of perfect periodicity. However, even with this allowance, the maximum simulated acceleration amplitude of the tested footbridge in the first vertical mode has been shown to overestimate the measured response twofold (equating to 200% error; cf. Figure 18 (b) in [15]). However, when comparing the results of this paper with those of [15] certain factors must be borne in mind. For

example, differences in experimental conditions, i.e. properties of the tested bridges and experimental protocols – in particular excitation of the first vertical mode at 2.99 Hz by the second harmonic of force from four pedestrians in [14], and modelling, i.e. FEM in [15] and equivalent modal model herein. Previous work by Dang and Živanović [17] has found that the percentage difference in the average peak per cycle acceleration value of the structural response simulated based on force reconstructed from 19 MCS markers model, relative to the measured value, was within ±20% at 92% confidence level. However, the movement of a load along the structure was not considered therein since the pedestrian was walking on a treadmill placed at the midspan of a composite bridge.

It is reported in [46] that walking over a surface with negative gradient results in reduction in step length, which is consistent with data presented in Figure 21. This effect is not visible in Figure 22, presenting data from tests in which the subject walked with pacing frequency of 2 Hz. It seems this effect is particularly strong for pacing frequencies lower than those preferred for normal walking. Nevertheless, considering data in Table 4, the slope of the walking surface does not seem to have a clear influence on the results.

The main advancement of the current loading model is that the pedestrian force is obtained directly from the motion of a single AHRS attached to a pedestrian. Although the force reconstruction gives better results than any other model presented so far, errors in the amplitude of force can still be expected. Nevertheless, it has been shown in section 2.4.1 that the temporal congruence of the reconstructed and directly measured force is very good. Indeed, this might be the reason the proposed loading model performs so well. The main source of discrepancy in simulated response amplitudes in [15] was assigned to human-structure interaction, in particular additional damping from walking pedestrians unaccounted for in the adopted loading model of [16]. It was shown that better accuracy of the simulated response amplitudes could be obtained by increasing damping ratio of the considered vertical mode from 0.19% to 0.8%, which corresponds to 0.15% increase in damping ratio per pedestrian. Less accurate results were obtained by running the simulations based on this assumption for all tests in the current study presented in section 5.1. Considering relatively low measured damping of mode 2 and 3 (see Table 3) there is some indirect evidence that, if the effect of additional damping is persistent, it is captured by the loading model. However, further work is necessary to gain confidence in this feature of the model.

Applying the oGRF reconstruction algorithm on average improved the magnitude of error in maximum amplitude of response for tests at mode 3 by 140% (see section 5.1.2), but detrimental results were obtain for mode 2, for which the magnitude of error increased by 43% (see section 5.1.1). Taking into account the results in Table 4 it may appear this step of the framework does not significantly (or in an obvious way) affect the results for the tests presented herein, but certain aspects of the experimental campaign need to be borne in mind in this assessment. Specifically, the pacing frequency of the pedestrian was enforced with a metronome providing strong stimulus for gait rhythmicity. This in turn can cause the

pedestrian velocity to be fairly constant, reducing the natural step-to-step variability in gate parameters captured by oGRF, which in turn reduces the difference between the results obtained by the two algorithms. Furthermore, because BB is relatively long and the considered mode shapes are of relatively low order (i.e. have few nodal points), the rate of change of the amplitude of modal force due to changing pedestrian location is generally slow and has relatively little influence on the response. For this reason it is expected that that the proposed procedure for reconstructing oGRF could bring considerable improvements of accuracy of the simulated response for shorter bridges.

When simulating the response of the bridge, the importance of accurate location tracking increases when oGRF is near a node. This is because the mode shape amplitude is almost null (near the node) but the rate of change of the modal amplitude is high. Therefore, in this region, small differences in location of the force can cause relatively high differences in the response calculated, i.e. the more nodal points the pedestrian crosses the more likely oGRF will give superior results. Another possible reason for the superior performance of the framework in mode 3 can be seen by examining modes 2 and 3 in Figure 19. The amplitude of mode shape 2 for the Northern section changes relatively slowly going from North to South, whereas the amplitude of mode shape 3 changes relatively quickly for the full length of the bridge. Both of the above are potential reasons for the better performance of the framework for mode 3 tests compared to mode 2 tests.

The same effect can be expected for tests in which pedestrian speed varies due to effects other than natural step-to-step variability, e.g. for walking in a crowd in which pedestrian gait patterns might be affected by close proximity of others, thus the assumption of linear progression of point of application of force is no longer substantiated. Another benefit of using the algorithm for reconstructing oGRF is when studying the behavior of individual pedestrians within a crowd of walkers. This is because the knowledge of pedestrian location relative to the location of other pedestrians and the mode shape is prerequisite for unveiling potential interaction mechanisms between different elements of crowd-structure system.

There are a number of limitations in the application/execution of the proposed framework, which need to be pointed out. More advanced PDR algorithms than used in this study are currently available [38]. For example, some of these algorithms account for drift in magnetometer readings associated with interference from magnetic fields other than that of the Earth (e.g. conducting wires or ferromagnetic materials used in construction), which can reduce heading errors. Other algorithms make better allowance of rolling motion of the foot during transition from stance to swing phase of gait in recognition of stationary periods in foot motion. It is expected the accuracy of the results obtained with (approximate) oGRF could be improved by using these algorithms. Nevertheless, it has been shown in this study, for the first time in the field of research concerned with the dynamic stability of structures, that a set of two AHRS can be used to obtain reliable data on pedestrian force and point of application of that force in situ.

6   Conclusions

The ambition of this study is to contribute to the development of a new class of pedestrian loading models, calibrated based on data representative of real pedestrian behaviour on full-scale structures. In order to accomplish this goal, a framework for the determination of localised pedestrian forces has been developed which uses wireless altitude and heading reference systems (AHRS). Importantly, in contrast to other models of structural loading on full-scale structures, the current framework does not require any extrapolations as to the temporal characteristics and amplitudes of pedestrian force. The framework relies on two main tasks:

- identification of pedestrian vertical loading from a single point inertial measurement taken from a suitable body landmark;

- determination of the point of application of pedestrian force based on data from a monitor attached to one foot.

To formulate the pedestrian vertical load model a dedicated experimental campaign was conducted during which six subjects walked on an instrumented treadmill at six speeds ranging from slow to normal, while instrumented with AHRS attached at the sternum, navel, lower back and seventh cervical vertebra. It has been shown that the force model built based on data from seventh cervical vertebra was able to yield an absolute error in the amplitude of the component of force at the pacing frequency of less than 15% at 90% confidence level. This is better than any other loading model presented so far. Furthermore, very good temporal congruence of the data reconstructed from the model with the benchmark data from the instrumented treadmill has been found, giving some confidence in applicability of the model for analysis of interactions in crowd-structure system.

An algorithm for the determining the origin of ground reaction force vector has been developed which utilises pedestrian dead reckoning and accounts for the bipedal nature of human gait. A single AHRS attached to one foot has been shown to be enough to accomplish this task for pedestrians walking on a footbridge which has one dominant direction of travel.

To validate the proposed modelling framework a dedicated experimental campaign was conducted on a full scale outdoor footbridge during which a pedestrian walked at frequencies of two vertical modes. Remarkably good match between the measured and simulated response of the bridge was found for both modes, accounting for the effect of the slope of the walking surface.

The developed framework allows the information of the behaviour of all components of crowd-structure system to be gathered thus allowing any emergent phenomena to be identified. Specifically, human-to-structure and human-to-human interactions are the core mechanisms assumed in many models of crowd behaviour and the associated structural loading to contribute to structural instability. These mechanisms

974 have so far escaped rigorous empirical verification. The developed framework could facilitate this
975 process.

982

References

983   **References**

984   [1]   J.H.G. Macdonald, Lateral excitation of bridges by balancing pedestrians, Proc. R. Soc. A Math.
985   Phys. Eng. Sci. 465 (2009) 1055–1073. doi:10.1098/rspa.2008.0367.

986   [2]   M. Bocian, J.H.G. Macdonald, J.F. Burn, Biomechanically inspired modelling of pedestrian-
987   induced forces on laterally oscillating structures, J. Sound Vib. 331 (2012) 3914–3929.
988   doi:10.1016/j.jsv.2012.03.023.

989   [3]   M. Bocian, J.H.G. Macdonald, J.F. Burn, Biomechanically inspired modeling of pedestrian-
990   induced vertical self-excited forces, J. Bridg. Eng. 18 (2013) 1336–1346.
991   doi:10.1061/(ASCE)BE.1943-5592.0000490.

992   [4]   A. McRobie, G. Morgenthal, D. Abrams, J. Prendergast, Parallels between wind and crowd
993   loading of bridges., Philos. Trans. A. Math. Phys. Eng. Sci. 371 (2013) 20120430.
994   doi:10.1098/rsta.2012.0430.

995   [5]   M. Bocian, J.H.G. Macdonald, J.F. Burn, Probabilistic criteria for lateral dynamic stability of
996   bridges under crowd loading, Comput. Struct. 136 (2014) 108–119.
997   doi:10.1016/j.compstruc.2014.02.003.

998   [6]   E.T. Ingólfsson, C.T. Georgakis, F. Ricciardelli, J. Jönsson, Experimental identification of
999   pedestrian-induced lateral forces on footbridges, J. Sound Vib. (2011) 1265–1284.
1000   doi:10.1016/j.jsv.2010.09.034.

1001   [7]   S.P. Carroll, J.S. Owen, M.F.M. Hussein, Experimental identification of the lateral human–
1002   structure interaction mechanism and assessment of the inverted-pendulum biomechanical model,
1003   J. Sound Vib. 333 (2014) 5865–5884. doi:10.1016/j.jsv.2014.06.022.

1004   [8]   M. Bocian, J.H.G. Macdonald, J.F. Burn, D. Redmill, Experimental identification of the behaviour
1005   of and lateral forces from freely-walking pedestrians on laterally oscillating structures in a virtual
1006   reality environment, Eng. Struct. 105 (2015) 62–76. doi:10.1016/j.engstruct.2015.09.043.

1007   [9]   M. Bocian, Determination of the self-excited forces on structures due to walking pedestrians using
1008   a biologically-inspired approach, PhD thesis, University of Bristol, 2014.

1009   [10]   S.-H. Kim, K.-I. Cho, M.-S. Choi, J.-Y. Lim, Development of human body model for the dynamic
1010   analysis of footbridges under pedestrian induced excitation, Int. J. Steel Struct. 8 (2008) 333–345.

1011   [11]   V. Racic, A. Pavic, J.M.W. Brownjohn, Experimental identification and analytical modelling of
1012   human walking forces: Literature review, J. Sound Vib. 326 (2009) 1–49.
1013   doi:10.1016/j.jsv.2009.04.020.

1014   [12]   E.T. Ingólfsson, C.T. Georgakis, J. Jönsson, Pedestrian-induced lateral vibrations of footbridges:
1015   A literature review, Eng. Struct. 45 (2012) 21–52. doi:10.1016/j.engstruct.2012.05.038.

1016   [13]   M. Haghighi, M. Bocian, O. Oddbjornsson, J.H.G. Macdonald, J.F. Burn, Synchronous data
1017   acquisition from large-scale clustered wireless sensor networks, APWCS 2013 - 10th IEEE Veh.
1018   Technol. Soc. Asia Pacific Wirel. Commun. Symp. 22-23 August 2013, Seoul, Korea. (2013).

1019   [14]   P. Dallard, T. Fitzpatrick, A. Flint, A. Low, R. Ridsdill Smith, M.R. Willford, M. Roche, London
1020   Millenium Bridge: Pedestrian-Induced lateral Vibration, ASCE J. Bridg. Eng. 6 (2001) 412–417.

[15] K. Van Nimmen, G. Lombaert, I. Jonkers, G. De Roeck, P. Van den Broeck, Characterisation of walking loads by 3D inertial motion tracking, J. Sound Vib. 333 (2014) 5212–5226. doi:10.1016/j.jsv.2014.05.022.

[16] Q. Li, J. Fan, J. Nie, Q. Li, Y. Chen, Crowd-induced random vibration of footbridge and vibration control using multiple tuned mass dampers, J. Sound Vib. 329 (2010) 4068–4092. doi:10.1016/j.jsv.2010.04.013.

[17] H.V. Dang, S. Živanović, Experimental characterisation of walking locomotion on rigid level surfaces using motion capture system, Eng. Struct. 91 (2015) 141–154. doi:10.1016/j.engstruct.2015.03.003.

[18] Winter, D.A., Biomechanics and motor control of human movement, 4th ed., Hoboken, USA, John Wiley & Sons, Inc., 1990.

[19] V. Racic, J.M.W. Brownjohn, A. Pavic, Reproduction and application of human bouncing and jumping forces from visual marker data, J. Sound Vib. 329 (2010) 3397–3416. doi:10.1016/j.jsv.2010.02.021.

[20] V. Racic, A. Pavic, J.M.W. Brownjohn, Modern facilities for experimental measurement of dynamic loads induced by humans: A literature review, Shock Vib. 20 (2013) 53–67. doi:10.3233/SAV-2012-0727.

[21] A. Pachi, T. Ji, Frequency and velocity of people walking, Struct. Eng. 83 (2005) 36–40.

[22] Medical Developpement, Analysis treadmil: ADAL 3D, http://www.medical-developpement.com/products/analysis-treadmill-adal-3d/, accessed on: 1/9/2015.

[23] APDM, Inc., Wearable sensors: the Opal, http://www.apdm.com/wearable-sensors/, accessed on: 1/9/2014.

[24] Codamotion, http://www.codamotion.com/, accessed on: 1/9/2014.

[25] S.O.H. Madgwick, A.J.L. Harrison, R. Vaidyanathan, Estimation of IMU and MARG orientation using a gradient descent algorithm, IEEE Int. Conf. Rehabil. Robot. (2011). doi:10.1109/ICORR.2011.5975346.

[26] S.P. Carroll, J.S. Owen, M.F.M. Hussein, Reproduction of lateral ground reaction forces from visual marker data and analysis of balance response while walking on a laterally oscillating deck, Eng. Struct. 49 (2013) 1034–1049. doi:10.1016/j.engstruct.2012.12.028.

[27] M.G. McDonald, S. Živanović, Measuring dynamic force of a jumping person by monitoring their body kinematics, RASD 2013 – 11th Int. Conf. Rec. Advanc. Struct. Dyn., Pisa, Italy, 2013.

[28] L. Tesio, V. Rota, C. Chessa, L. Perucca, The 3D path of body centre of mass during adult human walking on force treadmill, J. Biomech. 43 (2010) 938–944. doi:10.1016/j.jbiomech.2009.10.049.

[29] J.B. Kuipers, Quaternions and rotation sequences: A primer with applications to orbits, aerospace, and virtual reality, Princeton University Press, 2002.

[30] M.T. Taner, F. Koehler, Velocity spectra – digital computer derivation and applications of velocity functions, Geophysics. 34 (1969) 859. doi:10.1190/1.1440058.

| 1058 | [31] | National Health Service (NHS), Health survey for England - 2013 trend tables, London, UK, 2013. |
| 1059 | | |

1058 [31] National Health Service (NHS), Health survey for England - 2013 trend tables, London, UK,
1059 2013.

1060 [32] J.E. Bertram, A. Ruina, Multiple walking speed-frequency relations are predicted by constrained
1061 optimization, J. Theor. Biol. 209 (2001) 445–453.

1062 [33] M.H. Cole, W. Van Den Hoorn, J.K. Kavanagh, S. Morrison, P.W. Hodges, J.E. Smeathers, G.K.
1063 Kerr, Concurrent validity of accelerations measured using a tri-axial inertial measurement unit
1064 while walking on firm, compliant and uneven surfaces, PLoS One. 9 (2014) 1–12.
1065 doi:10.1371/journal.pone.0098395.

1066 [34] Y. Fujino, B.M. Pacheo, S.-I. Nakamura, P. Warnitchai, Synchronisation of human walking
1067 observed during lateral vibration of a congested pedestrian bridge, Earthq. Eng. Struct. Dyn. 22
1068 (1993) 741–758.

1069 [35] S. Nakamura, Field measurements of lateral vibration on a pedestrian suspension bridge, Struct.
1070 Eng. 81 (2003) 22–26.

1071 [36] Yoshida, J., Y. Fujino, Y., Sugiyama, T., Image processing for capturing motions of crowd and its
1072 application to pedestrian-induced lateral vibration of a footbridge, Shock Vib. 14 (2007) 251–260.

1073 [37] M.C. Araújo Jr, H.M.B.F. Brito, R.L. Pimentel, Experimental evaluation of synchronisation in
1074 footbridges due to crowd density, Struct. Eng. Int. 19 (2009) 298–303.
1075 doi:10.2749/101686609788957784.

1076 [38] R. Harle, A Survey of indoor inertial positioning systems for pedestrians, IEEE Commun. Surv.
1077 Tutorials. 15 (2013) 1281–1293.

1078 [39] X.Y.X. Yun, E.R. Bachmann, H. Moore, J. Calusdian, Self-contained position tracking of human
1079 movement using small inertial/magnetic sensor modules, Proc. 2007 IEEE Int. Conf. Robot.
1080 Autom. (2007). doi:10.1109/ROBOT.2007.363845.

1081 [40] E. Foxlin, Pedestrian tracking with shoe-mounted inertial sensors, IEEE Comput. Graph. Appl. 25
1082 (2005) 38–46. doi:10.1109/MCG.2005.140.

1083 [41] J.M.W. Brownjohn, F. Magalhães, E. Caetano, A. Cunha, Ambient vibration re-testing and
1084 operational modal analysis of the Humber Bridge, Eng. Struct. 32 (2010) 2003–2018.

1085 [42] J.M.W. Brownjohn, P. Reynolds, S.K. Au, D. Hester, M. Bocian, Experimental modal analysis of
1086 civil structures: State of the art, in: 7th Int. Conf. Struct. Heal. Monit. Intell. Infrastruct., Turin,
1087 Italy, 2015.

1088 [43] D.J. Ewins, Modal testing: Theory, practice and application, 2nd ed., Baldock, England, Research
1089 Studies Press, Ltd., 2000.

1090 [44] H. Bachmann, A.J. Pretlove, J.H. Rayner, Vibrations induced by people, in: Vibration problems in
1091 structures: practical guidelines, (1995) 1–28. doi:10.1007/978-3-0348-9231-5.

1092 [45] BSI, BS EN 1991-1-2 Eurocode 1. Actions on structures - Part 2: Traffic loads on bridges, British
1093 Standards Institution, 2003.

1094   [46]   J. Sun, M. Walters, N. Svenson, D. Lloyd, The influence of surface slope on human gait
1095   characteristics: a study of urban pedestrians walking on an inclined surface, Ergonomics. 39
1096   (1996) 677–692. doi:10.1080/00140139608964489.

1097 **Nomenclature**

1098 AHRS – altitude and heading reference system

1099 BB – Baker Bridge

1100 C7 – seventh cervical vertebra

1101 FEM – finite element model

1102 GRF – ground reaction force

1103 LB – lower back

1104 LCS – local coordinate system

1105 MCS – motion capture system

1106 N – navel

1107 oGRF – origin of the ground reaction force vector

1108 PDR – pedestrian dead reckoning

1109 QA – Honeywell accelerometer

1110 S – sternum

1111 TD – touch-down of the foot with the ground

1112 TO – take-off of the foot from the ground

1113 WCS – world coordinate system

1114 ZUPT – zero velocity update